THE ASTRONOMICAL JOURNAL VOLUME 108, NUMBER 3 SEPTEMBER 1994

THE OPTICAL AND NEAR-INFRARED COLORS OF GALAXIES. I. THE PHOTOMETRIC DATA[1]

MATTHEW A. BERSHADY[2,3]

Department of Astronomy and Astrophysics, The University of Chicago, 5640 S. Ellis Ave., Chicago, Illinois 60637 and University of California Observatories/Lick Observatory, University of California, Santa Cruz, California 95064
Electronic mail: mab@lick.ucsc.edu

MARK HERELD[2]

Department of Astronomy and Astrophysics, The University of Chicago, 5640 S. Ellis Ave., Chicago, Illinois 60637
Electronic mail: hereld@oddjob.uchicago.edu

RICHARD G. KRON[2]

Fermi National Accelerator Laboratory, MS 127, Box 500, Batavia, Illinois 60510
Electronic mail: rich@oddjob.uchicago.edu

DAVID C. KOO[2]

University of California Observatories/Lick Observatory, Board of Studies in Astronomy and Astrophysics, University of California, Santa Cruz, California 95064
Electronic mail: koo@lick.ucsc.edu

JEFFREY A. MUNN[2]

Yerkes Observatory, The University of Chicago, P.O. Box 0258, Williams Bay, Wisconsin 53191-0258
Electronic mail: jam@yerkes.uchicago.edu

STEVEN R. MAJEWSKI[2,3]

The Observatories of the Carnegie Institution of Washington, 813 Santa Barbara St., Pasadena, California 91101
Electronic mail: srm@ociw.edu

Received 1992 August 14; revised 1993 December 15

ABSTRACT

We present optical and near-infrared photometry and spectroscopic redshifts of a well defined sample of 171 field galaxies selected from three high galactic latitude fields. This data set forms the basis for subsequent studies to characterize the trends, dispersion, and evolution of rest-frame colors and image structure. A subset of 143 galaxies constitutes a magnitude-limited sample to $B\sim19.9-20.75$ (depending on field), with a median redshift of 0.14, and a maximum redshift of 0.54. This subset is statistically representative in its sampling of the apparent color distribution of galaxies. Thirty six galaxies were selected to have the reddest red-optical colors in two redshift intervals between $0.2<z<0.3$. Photometric passbands are similar to *U, B, V, I*, and *K*, and sample galaxy spectral energy distributions between 0.37 and 2.2 μm in the observed frame, or down to 0.26 μm in the rest frame for the most distant galaxies. *B* and *K* images of the entire sample are assembled to form the first optical and near-infrared atlas of a statistically-representative sample of field galaxies. We discuss techniques for faint field-galaxy photometry, including a working definition of a total magnitude, and a method for matching magnitudes in different passbands and different seeing conditions to ensure reliable, integrated colors. Photographic saturation, which substantially affects the brightest 12% of our sample in the optical bands, is corrected with a model employing measured plate-density distributions for each galaxy, calibrated via similar measurements for stars as a function of known saturation level. Both the relative and absolute calibration of our photometry are demonstrated.

1. INTRODUCTION

The original goal of this project was to measure the evolution of the optical and near-infrared colors of fields galaxies out to cosmologically-interesting redshifts. This was motivated theoretically by the work of Wyse (1985), Renzini & Buzzoni (1986), and Choksi & Wright (1987) which brought attention to changes with age in post-main-sequence stellar populations and the possible subsequent effects on the integrated near-infrared light of galaxies.

At the same time we were aware that the result of Ellis & Allen (1983), who found unexpectedly high redshifts on the basis of near-infrared colors for an optically selected sample of faint galaxies, was dependent on our knowledge of the intrinsic range of rest-frame galaxy colors. With the advent of infrared array detectors in the late 1980's, a new generation of deep *K* band surveys began to discover objects whose

[1]Submitted in partial fulfillment of the requirements for the degree of Doctor of Philosophy, The University of Chicago.
[2]Visiting Astronomer, Kitt Peak National Observatory, National Optical Astronomy Observatories, which is operated by the Association of Universities for Research in Astronomy, Incorporated, under cooperative agreement with the National Science Foundation.
[3]Hubble Fellow.

 0004-6256/94/108(3)/870/26/$0.90

colors and number densities did not clearly have local counterparts (Elston *et al.* 1988, 1989; Cowie *et al.* 1988), although these surveys were largely without redshifts. The analysis of more recent spectroscopic surveys including these same objects (Lilly *et al.* 1991; Cowie *et al.* 1992) has not resolved their relation to galaxy populations in the local universe.

The availability of a large sample of optically-selected field galaxies with spectroscopic redshifts (Koo & Kron 1988b) led us to embark upon a K band imaging survey of this sample to further determine the redshift dependence of the optical and near-infrared colors of galaxies. At the same time, we hoped to exploit the new infrared imaging arrays to investigate the relationship between the morphology and colors of distant galaxies.

It quickly became apparent to us (Bershady *et al.* 1990) that the range of optical–near-infrared colors at a given redshift was larger than anticipated from existing evolution models (e.g., Bruzual 1981). In particular, we found that color–luminosity effects existed in the optical–near-infrared colors. This effect is well known for nearby galaxies (Visvanathan 1981; Wyse 1982; Tully *et al.* 1982), and the presence of this effect at larger redshifts was anticipated by the work of Mobasher *et al.* (1986). Hence before changes in galaxy colors with redshift can be explored, independent of understanding a survey's selection function and establishing accurate κ-corrections, it is necessary to determine the intrinsic range of galaxy colors in the rest frame.

Here and in a second paper, (Bershady 1994, hereafter referred to as Paper II), we will present a study of the range and dispersion in the colors of our field galaxy sample. This is the first substantial effort to use a sample at intermediate redshift to check the expectations for the number–color–redshift relation, $A(c,z)$, for galaxies based on properties of local galaxies. The redshifts of our sample are large enough so that the colors are substantially affected, but small enough that image structure can still be studied.

This paper addresses the construction and calibration of a photometric database of apparent galaxy colors and total magnitudes. In Sec. 2 we describe and define our galaxy sample selection and completeness. Section 3 contains a thorough description of all aspects of the photometric data and calibration. To give a more detailed guide to the reader, introductions are provided in the beginning of this section as well as in Secs. *3.2* (photometric apertures), *3.3* (photometric zero-points), and *3.4* (photographic saturation). For those interested only in an overview of the main aspects of the photometric procedure, summaries are provided at the end of Secs. *3.2* and *3.4*. Total magnitudes, colors, and spectroscopic redshifts are presented in Sec. 4, in addition to photographic J (similar to Johnson B) and K images of all galaxies in our sample. Section 5 contains a brief discussion of the color–color and color–redshift distribution for this galaxy sample. A summary of the results of this work is found in Sec. 6. The spectral classification and an exploration of the rest-frame properties of color and luminosity of our galaxy sample are pursued in Paper II. Future work will address galaxy image structure as well as evolution of the galaxy population with redshift.

TABLE 1. Fields.

Field Name	Catalogue Center (1950) α	δ	Area[a] deg.^{2}	csc|b|[b]	E(B-V)[c]
SA68	$00^h14^m53^s$	+15°36′.5	0.214	1.385	0.00-0.10
SA57	$13^h06^m15^s$	+29°39′.1	0.284	1.003	0.00-0.05
Herc-1	$17^h18^m58^s$	+49°58′.4	0.384	1.753	0.00-0.05

Notes to TABLE 1

[a] Areas are from Koo (1986) for SA57 and SA68, and from Kron *et al.* (1991) for Herc-1.
[b] The galactic lattitude, b.
[c] Galactic reddening as estimated from maps of Burstein & Heiles (1982) and Boulanger & Perault (1989).

2. SAMPLE SELECTION AND COMPLETENESS

The field galaxy sample studied here is defined by our K band imaging survey (Bershady *et al.* 1990). The sample was selected from optical, multicolor catalogues of three, high-latitude fields centered on Selected Areas 57 and 68 (SA57 and SA68), and Hercules 1 (Herc-1, an area selected by Kron). SA57 and SA68 are circular fields approximately 40 arcmin in diameter, corresponding to the usable portion of the Mayall 4 m telescope prime-focus plates from which catalogues were generated. The Herc-1 field is square, and covers a comparable area. Field centers and areas are given in Table 1. The photographic photometry in the catalogues consists of U, J, F, and N bands, which are similar to U, B, V or R, and I, respectively. The photographic system has been defined by Kron (1980) for the J and F bands, and by Koo (1986) for the U and N bands. Majewski (1992) has made a considerable effort to improve both the transformations between photographic and standard systems, as well as the photographic zero-points.

The three fields from which we draw our sample have by now received considerable attention. For example, the catalogues and Mayall 4 m plate collection have been used to study faint galaxy populations in SA57 and SA68 (Kron 1980; Koo 1986; Koo *et al.* 1986a), radio galaxies in all fields (Windhorst *et al.* 1984), quasistellar populations in all fields (Kron & Chiu 1981; Koo & Kron 1982; Koo *et al.* 1986a; Koo & Kron 1988a; Kron *et al.* 1991), variable objects in SA57 (Trevese *et al.* 1989; Bershady *et al.* 1991; Majewski *et al.* 1991), and galactic stellar populations in SA57 (Majewski 1992).

The catalogues in SA57 and SA68 were made by Kron and Koo using the finding algorithm of Kron (Kron 1980; Koo 1986), and by Munn and Majewski (Munn *et al.* 1994) for Herc-1 using FOCAS (Valdes 1982). The catalogues provide reliable and complete object lists, in particular for bright galaxies. To weed out spurious detections, objects were required to be found on either two J or two F plates for SA57 and SA68, or three of the seven plates used for the Herc-1 catalogue (one U, two J, two F, and two N plates). To the depth of our survey, no galaxies should be lost due to misclassification: the star–galaxy separation is excellent to $J \leq 21.5$, and the compact blue galaxies with stellar morphology found in our QSO surveys (Koo *et al.* 1994) are typically fainter. For bright galaxies, the catalogues were reviewed by hand to restore extended objects split into multiple components by the finding algorithms. There has been no rigorous test to see whether any class of objects has been

excluded, e.g., low surface-brightness, extended objects. In Herc-1, all such objects found by eye (M.A.B.) from inspection of the plates were included in the catalogue. In SA57 and SA68, Kron's finding algorithm should identify objects with central surface brightness down to 0.2% of the sky background (in the J or F bands). Extended objects with surface brightness gradients larger than 1% over scales $\leqslant 6$ arcsec will also be found.

The plates, their digitization, and the photometric properties of the catalogues are discussed in detail in Sec. 3. Here we are concerned specifically with defining the sample selection in terms of total magnitudes in the optical bands. To first order, differences between the two finding and photometry algorithms used to create the catalogues (Kron vs FOCAS) do not affect the sample definition since the faintest levels of the present survey are substantially above the plate limit. Since one result of this study is uniformly calibrated galaxy photometry across the three fields, second order corrections to sample limits due to different photometric algorithms and zero-point corrections have been calculated and applied *a posteriori*. We note here that for Herc-1, FOCAS total magnitudes were used when defining the sample, even though fixed aperture photometry was used in the ensuing color analysis. FOCAS total magnitudes were the closest estimates of true total magnitudes available for sample selection in this field.[4] The aperture magnitudes (2 arcsec radii) are as much as 1.5, but typically 0.3, mag fainter than galaxy isophotal magnitudes for $J_{\rm total}<20.5$, and therefore are not suitable for estimates of total magnitudes (Fig. 4 illustrates the difference between aperture and total magnitudes for the K band). An offset of -0.2 mag has been applied to the SA57 magnitudes when defining the sample. This offset is a correction which compensates in the mean for systematically smaller optical apertures used in SA57 relative to SA68, as described in Sec. *3.2.3*. Table 2 presents the survey limits using our best estimates of total magnitudes. These magnitudes are uniformly calibrated across the three fields.

Galaxies were selected from two subsamples. The largest subsample of 143 galaxies is limited by J magnitude. Galaxies brighter than the magnitude limits listed in Table 2(a) were imaged in the K band (Sec. *3.1.3*) only if they had reliable redshifts, with a few exceptions. Preference for galaxies with known redshifts was the most effective use of observing time given our interest in rest-frame colors. However, for statistical studies of the properties of galaxies, it is critical to understand the completeness and potential biases in the sample selection. We turn to this issue in a moment. Table 2(a) lists the total number of galaxies, the number of galaxies with redshifts, and the number of galaxies with K band photometry to the respective J magnitude limits for each field. Different limits reflect the amount of available observing time and the intrinsic number of galaxies per field. In SA68 and Herc-1, the number of galaxies with redshifts exceeds those with K photometry because of recent acquisitions of new redshifts.

TABLE 2(a). The magnitude-limited sample.

			Number of Galaxies				
Field	$\leqslant J^a$	$z_{\rm median}$	total	redshifts	(%)	K photometry	(%)
SA68	20.5	0.153	63	51	(81)	46	(73)
SA57	19.65[b]	0.123	49	46	(94)	47[c]	(96)
Herc-1	20.5	0.139	181	125	(69)	50[d]	(28)

Notes to TABLE 2(a)

[a]All magnitude limits are expressed as total magnitudes that include zero-point corrections to original catalogues (Sec. *3.4.1*). SA57 and SA68 total magnitudes are defined by circular apertures of radius $2r_1$, as discussed in Sec. *3.2*. Herc-1 total magnitudes (from FOCAS) are defined in Sec. 2.
[b]SA57 magnitude limit is corrected in the mean for the aperture effect discussed in Sec. *3.2.3*.
[c]Number includes 2 galaxies with uncertain redshifts, 2 galaxies without U and N photometry, and 1 galaxy with uncertain K photometry.
[d]Number includes 3 galaxies with uncertain redshifts and 3 galaxies with uncertain K photometry.

TABLE 2(b). The color–redshift selected sample.[a,b]

				Number of Galaxies[c]			
Field	redshift range	$\leqslant K_{\rm sim}$	$\leqslant F$	total	redshifts	(%)	K photometry
SA68	$0.29\leqslant z\leqslant 0.33$	17.7	20.5	254	116	(46)	19
SA57	$0.21<z<0.26$	15.85	19.75	105	55	(52)	17

Notes to TABLE 2(b)

[a]The color–magnitude limit $K_{\rm sim}\equiv F-2.45(F-N)-0.75$ is a reasonable estimate of the K magnitude. An additional limit is imposed in the F band.
[b]Magnitudes and corrections to the magnitudes used to define the sample limits are the same as described in the notes to Table 2(a).
[c]Except for the counts of galaxies with K photometry, galaxy counts are for all redshifts. The galaxies with K band photometry include 3 galaxies in the magnitude limited sample of SA68 and 5 galaxies in the magnitude limited sample of SA57 [Table 2(a)].

In an effort to probe to redshifts higher than those afforded by typical $J\sim 20$ galaxies, a second subsample of 36 galaxies was selected by taking advantage of the large-scale structure observed in our fields. In SA57 and SA68, galaxies in redshift "spikes" between $0.2<z<0.3$ were photometered in order of their predicted K band magnitudes. These estimates were made empirically from our initial magnitude-limited survey on the basis of correlations between K, F, and N magnitudes. In essence, this is a magnitude-, color-, and redshift-limited sample, however the selection is nontrivial. We have included in Table 2(b) the total number of galaxies as well as the number of galaxies with redshifts for the appropriate fields to the effective F magnitude and $F-N$ color limits imposed at the redshift spikes of the K band survey. This information can be used to estimate our completeness. Eight galaxies in this subsample are also in the first, magnitude-limited subsample.

Five galaxies with measured redshifts were observed serendipitously because of their angular proximity to our primary targets. Two of these objects have somewhat uncertain

[4]FOCAS total magnitudes are defined by apertures based on an isophotal shape for each object. For the Herc-1 catalogue this shape is defined by all contiguous pixels above a noise threshold in an image smoothed with a 5×5 pixel kernel (0.37 arcsec per pixel). This corresponds to isophotes fainter than $\mu(J)=29.5$ mag per arcsec^2 on the original image for objects brighter than $J=20.5$. To construct the total aperture, FOCAS fills the concavities of this shape and isomorphically doubles the area of the resulting aperture (Valdes 1982).

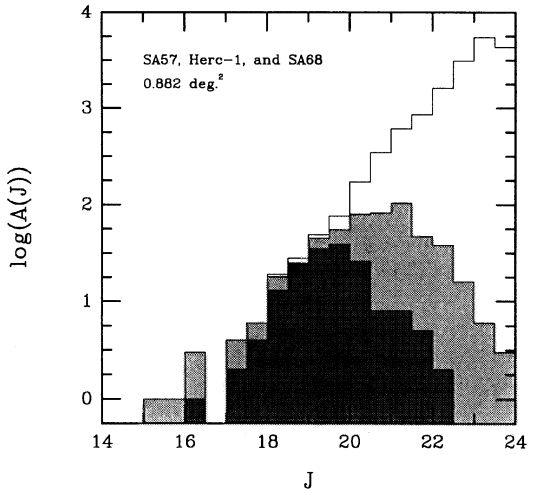

FIG. 1. The completeness of the redshift and K band surveys for all three fields, combined, is plotted as a function of J magnitude for the differential counts in bins of 0.5 mag: K band survey (dark-filled histogram); redshift survey (light-filled histogram); all galaxies (open histogram).

redshifts. All five objects, which span a wide range of apparent magnitude and redshift, are included in our data tables for general interest, but are not used in any statistical analysis.

The numerical and statistical completeness of our galaxy sample is illustrated in Figs. 1 and 2. The first figure, a histogram of the galaxies per 0.5 mag in the J band for all galaxies, galaxies with redshifts, and galaxies in the K band survey, can be used to directly compute the survey completeness. The numerical completeness of the K band and redshift

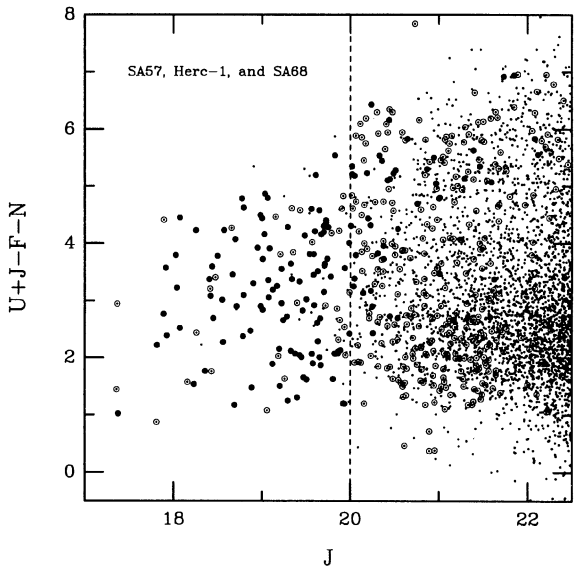

FIG. 2. The statistical completeness of the redshift and K band surveys for all three fields combined is displayed in the color–magnitude diagram of $U+J-F-N$ vs J. Filled dots represent the K band survey galaxies; open dots represent the redshift survey galaxies; points represent remaining galaxies in the photometric catalogues. The dashed line at $J=20$ is the approximate limit of our statistical completeness.

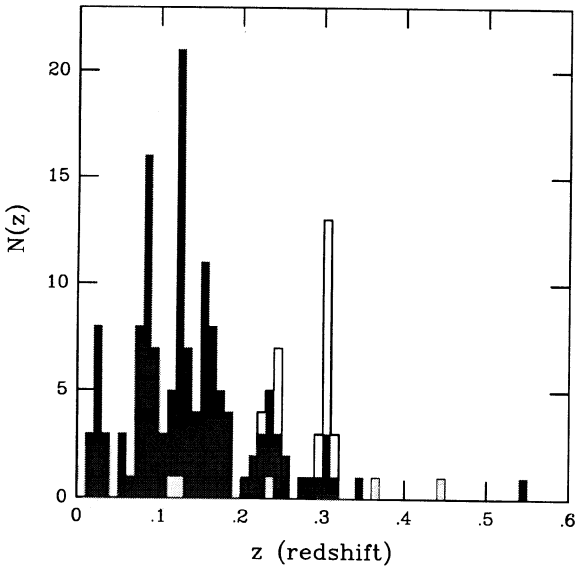

FIG. 3. Counts per 0.01 redshift interval vs redshift for galaxies in magnitude-limited sample [dark-filled histogram, Table 2(a)], color–redshift selected sample [open histogram and thick solid line, Table 2(b)], and serendipitous objects (light-filled histogram and thin solid line).

surveys is very high at bright magnitudes. The differential counts fall below 50% only fainter than $J=20$ for the K band survey, while the redshift survey goes roughly 0.25–0.5 mag fainter to this level of completeness. Figure 2 shows the distribution in color and magnitude for the same samples. The color index $U+J-F-N$ is useful for separating the galaxy distribution into color classes because of the long baseline representing $\Delta\lambda/\lambda\sim0.75$ (Koo 1985). Note that for $J<20$, the color distribution is both well and evenly sampled; the redshift and K band surveys are statistically complete. At fainter magnitudes, the redshift survey is biased towards bluer galaxies. This is largely because of a new, color-selected survey in SA68 by Smetanka (1993). The K band survey is naturally biased towards redder galaxies, since this is the realm of the color–redshift selected subsample.

In summary, at brighter magnitudes we have a sample which well represents the observed galaxy color distribution. At fainter magnitudes we have sampled the reddest galaxies in two specific intervals of redshift centered at $z=0.24$ and $z=0.3$. The total sample, not counting serendipitously observed objects, includes 171 galaxies, of which over 97% have high-quality U, J, F, N, and K magnitudes as well as reliable spectroscopic redshifts. The redshift distribution is illustrated in Fig. 3.

3. OPTICAL AND NEAR-INFRARED PHOTOMETRY

In this section we describe the salient aspects of our data set and discuss the reduction and calibration procedures most significant to ensuring the accuracy of our photometry. The organization is by procedural order. In Sec. *3.1* we outline the photometric and spectroscopic observations, and discuss the data set and photometric reductions. Particular attention

TABLE 3. Hercules 1 catalog plate set.

MPF	Corrector	Emulsion	Filter	Exposure (minutes)	α(1950)	δ(1950)	U.T. (start)	H.A. (end)	Principal Observer	Date (U.T.)
3324	UBK-7	IIIa-J	UG5	145	17:18:58.0	49:58:00	-	-	Koo	5/18/90
4042	UBK-7	IIIa-J	GG385	50	17:18:58.1	49:57:56	03:01.0	2W29	Majewski	9/12/85
4043	UBK-7	IIIa-J	GG385	50	17:18:57.5	49:57:56	03:53.0	3W22	Majewski	9/12/85
1574	BK-7	127-02	GG495	60	17:18:08.0	49:59:10	10:49.2	0E05	Kron	4/5/75
4044	UBK-7	IIIa-F	GG495	65	17:18:57.0	49:57:52	94:49.0	4W33	Majewski	9/12/85
3159	BK-7	IV-N	RG695	50	17:18:58.0	49:58:00	02:48.6	1W12	Koo	8/28/79
4174	UBK-7	IV-N	RG695	70	17:18:58.0	49:58:02	10:15.0	0W34	Majewski	4/20/88

is paid to the K band imaging survey, which is the latest addition to the data set. Section *3.2* describes the specific photometric procedure used to determine instrumental magnitudes well matched across the different bands, photometric material, and observing conditions. This entails consideration of photometric aperture selection as well as the method of calibration for galaxies. We also demonstrate that distance-dependent systematics on our measured total magnitudes and integrated colors are negligible. The absolute calibration of our photometry is established in Sec. *3.3*. In Sec. *3.4* we determine whether photographic saturation affects the photometry of some of our brightest galaxies. We proceed to derive a saturation correction and demonstrate the correction's accuracy. Galactic extinction is discussed in Sec. *3.5*. The final photometry, redshifts, and images are presented in Sec. 4.

3.1 Observations and Image Processing

3.1.1 Optical photometry

Photographic plates in the U, J, F, and N photographic bands have been acquired over the last 18 years principally by Kron, Koo, and Majewski using the prime focus of the Mayall 4 m telescope at Kitt Peak. Many of these plates have been used to construct the photometry catalogues, described in the previous section, from which we have selected our objects. These plates are listed by Koo (1986) for SA57 and SA68, and we list the plates used in the Herc-1 photometric catalogue in Table 3. The plate scans used to construct these catalogues used an aperture and step size of 20 μm, or 0.37 arcsec.

Additional photometric catalogues in SA57 have been produced with independent plate scans and linearization schemes, using a pixel size of 0.28 arcsec, as described by Koo *et al.* (1986b). Subsequent work by Trevese and Nanni have resulted in catalogues for a large fraction of the entire SA57 plate collection. A subset of these catalogues (hereafter referred to as Rome) was kindly made available by Trevese. The Rome catalogues were used to extract U, J, F, and N photometry for 15 of the brightest galaxies in SA57, as well as to conduct other photometric tests, discussed in later sections (for historical reasons, the bright galaxies in SA57 lacked U and N magnitudes in the Koo–Kron catalogue, as well as radial moments, r_1, from which we define a photometric aperture, as discussed in Sec. *3.2.1*). For reference, in SA57 we used Rome catalogues of plates mpf 3920 (U), 2176, 3313, and 3919 (J), 3922 (F), and 3923 (N), which are listed in Table 2 of Majewski (1992).

The Rome catalogues are based on plate scans transformed from density (or transmission) to intensity via a linearization technique that utilizes the isomorphic nature of stellar profiles (Nanni *et al.* 1980; Koo *et al.* 1986b). A similar linearization technique is used by Infante & Pritchet (1992) in their photographic survey of the North Galactic Pole. This technique is independent of the plate calibration spots used in the construction of our other catalogues. In principle, a linearization process employing stellar profiles should be superior to using the calibration spots, and should increase the dynamic range over which the plates reliably can be linearized, particularly at high densities. This is important for our work because some of the very brightest galaxies are saturated in their image cores. Tests for saturation are discussed in Sec. *3.4*.

Starting in 1986, Koo, Kron, and Majewski began deep U, B, V, R, and I band CCD observations using the prime focus of the 4 m Mayall telescope in small regions of the same fields. These data are used here for calibration.

3.1.2 Redshifts

Redshifts in our fields have been collected over the last decade primarily with the Mayall telescope and both the CRYOCAM and RC spectrographs with the various generations of multi-object systems (Koo & Kron 1988b). Galaxies were originally selected using the F instead of the J band because galaxy κ-corrections are expected to be smaller in redder bands and CCD sensitivity is generally greater (the N band was not used because N plates are generally not as deep as J or F plates, and the sky background is substantially higher). In more recent surveys of QSOs (Kron *et al.* 1991), narrow-emission-line objects, and large-scale structure (Koo *et al.* 1992), there has been the opportunity to fill in redshifts for brighter galaxies limited by J magnitude.

A reliability index is assigned to the spectroscopic redshifts deduced from these data. For this work, unless otherwise noted, we use only redshifts for objects which were judged to have greater than 50% probability of being correct. In practice this means that *at least* one feature has been definitely detected. Typically, two or more features are identified. Seven objects have uncertain spectroscopic redshifts. However their redshifts agree with redshifts derived from colors (Koo 1985) to within the accuracy of the latter estimates. For one object without a spectroscopic redshift (herc1.4389), we have adopted a color-estimated redshift.

3.1.3 K band imaging survey

The latest addition to the data set is a K band imaging survey of the bright, magnitude-limited and faint, color-selected galaxy samples studied in this work (Bershady *et al.* 1990). K band images were taken primarily using the Mayall

4 m telescope with the IRIM over a period of fifteen nights from September 1988 through May of 1990. The IRIM used a Santa Barbara Research Corporation 62×58 InSb imaging array with a reimaged pixel scale of 0.4 arcsec per pixel, which is well matched to the optical plate scans. We were extremely fortunate to have photometric conditions on eleven of these nights, with good to excellent seeing conditions, characteristically just under one arcsecond. This allowed us to calibrate our photometry typically to within 1%.

Over 170 program galaxies were observed during this period, with average total magnitude of $K=15.1$. Most relevant for the study at hand, the resulting random photometric errors for the total K band magnitudes (typical aperture radii of 3.5 arcsec) are very good: over half the sample has random errors less than 0.06 mag, and over 90% of the sample has random errors less than 0.15 mag. The distribution of random photometric errors in the U and N bands for this sample are comparable.

Although this was a "pointed" survey, namely fields were selected on the basis of previously known objects, the survey can also be characterized by its coverage of 60 sq arcmin to an average depth of $K=21.1$ mag per sq arcsec for a 1σ detection. As a result, we serendipitously obtained photometry for over 900 objects matched to our optical catalogues. About 230 of these objects have usable photometry (errors less than 0.3 mag). This has yielded an important subsample of galactic stars which will be used to check our color zero-points in Sec. *3.3*. Analysis of serendipitously observed field galaxies without redshifts will be presented in a future paper; this set represents a K magnitude-limited sample.

K band images for a smaller, overlapping subset of galaxies with $J<19$ were taken at Lick Observatory using the Shane 120 in. telescope and the Prototype Near-Infrared Camera (PNIC, Hereld *et al.* 1990). This camera used a Rockwell HgCdTe 64×64 imaging array with a plate scale of 0.67 arcsec per pixel.

The details of the image processing and photometry for both cameras were nearly identical, but extensive, and will be discussed in a future paper. The salient features of the image processing and photometry are summarized here for completeness.

The first step was to make a linearity correction to the raw IRIM images, similar to what is described by Storm *et al.* (1992). This resulted in a net correction of 8% to the final background-limited photometry. Images were processed by subtracting medians of 5 to 10 neighboring, disregistered, object frames that were first dark subtracted and scaled to a common sky level before the median filter was applied. Flat-field frames were constructed from night-long averages of these local medians. Cosmic rays were not removed because object flux was invariably lost when any statistical removal scheme was applied, and the 4000 frames of our survey made the task of removing them by hand unreasonable. However the energy spectrum of the cosmic rays was measured, from which we estimated they did not significantly contaminate the photometry.

After processing, images were first registered on the basis of telescope guider offsets, and then cross-correlated for finer registration. Once the images were centered, photometry was carried out on the individual images in order to measure directly the flux variance independently of estimates based on the background noise. These two error measurements were found to agree to better than 10% for all except the largest apertures, where the difference was 30%. However, the *measurement* of the background noise is more accurate than the *measurement* of the flux variance (the background is brighter than the object, and there are more pixels sampling the background flux than images sampling the object flux). Therefore, we adopted the background noise estimate, corrected in the mean to agree with the variance determined directly from the flux measurements.

Finally, we calibrated our data with photometry of 11 of the stars from Elias *et al.* (1982; hereafter this paper is referred to as defining the California Institute of Technology, CIT, standard near-infrared system), including GI406. The latter is sufficiently red to allow us to make some estimate of a possible color term with respect to the CIT standard near-infrared system. None was found to better than 1% in either $J-K$ or $H-K$, which is confirmed by our further investigation of the optical–infrared color zero-points in Sec. *3.3*. Four galaxies included in our sample were photometered only under considerably nonphotometric weather or detector conditions. Care has been taken to appropriately estimate the uncertainty in this photometry, and these objects are indicated in Table 6 (Sec. 4). The resulting, overall galaxy photometry is uniform, well calibrated, and has good estimates for both the most probable K magnitude *and* error.

3.2 Photometric Apertures

Galaxy photometry can be particularly treacherous, and here we take care to define our photometric technique. We are interested in both an estimate of total galaxy flux, to set a physical scale, as well as the *integrated* colors. To accomplish these aims, we ostensibly adopt the photometric technique of Kron (1980) to measure a total magnitude. However, the addition of the K band data, as well as some nonuniformity in the existing optical photometry, has led to some modifications of Kron's technique. This development warrants an explication of the calibration process for extended object photometry. Our method is designed to minimize potential systematics in the derived *instrumental* colors of galaxies at the sacrifice of a reasonable increase in random photometric error. In the next four subsections we discuss in turn the selection of photometric apertures to measure the total magnitudes of galaxies, photometric systematics that depend on galaxy type as well as measuring algorithm, the application of a standard aperture which is meant to measure a total magnitude, and finally the method of instrumental calibration. In Sec. *3.2.5* we demonstrate that systematics effects due to color gradients on the integrated colors for our galaxies are likely to be negligible. We summarize our photometric procedure in Sec. *3.2.6*.

3.2.1 Aperture selection

The difficulty in photometering galaxies is that unlike stars, galaxies have different and *a priori* unknown profiles. Even in identical seeing conditions, a fixed aperture will measure varying fractions of the total flux for galaxies of different apparent shape and size. The same aperture will measure another, but constant, fraction for stars, and unlike galaxy photometry, stellar photometry therefore is directly calibratable with other, standard stars. The problem is compounded for galaxy photometry of multiband, multi-image data where the seeing conditions are nonuniform. Sufficiently large apertures will minimize systematic differences between the fraction of total flux measured for different galaxies as well as different images of the same galaxy, but at the cost of lower signal-to-noise.

A sensible scheme can be developed either to calibrate the relation between a modest, fixed aperture to a total or standard aperture for each galaxy on the basis of some other information, such as the light distribution, or to use this same information to tailor an aperture for each galaxy to enclose a nearly total (and hopefully fixed) fraction of light. Neither option is simple. The former is in the tradition of single element aperture photometry, and falls prey to uncertainties in the adopted curve of growth (e.g., Sandage 1972) or analogously, the assumed shape of the light profile (e.g., Gunn & Oke 1975; Hoessel 1980). Several well defined schemes have been devised to determine total, or near-total apertures based on the light profiles of galaxies, e.g., Kron (1980), Ellis (1980), Tyson (1984, 1988), Koo *et al.* (1986b), Infante & Pritchet (1992), and Dressler & Gunn (1992). It is beyond the scope of this paper to compare these techniques. However, the technique that defines apertures based on a fixed isophote suffers from the effects of $(1+z)^{-4}$ surface brightness dimming. Hence the isophotal technique is problematic for distant galaxy work that covers a wide range of redshift and apparent magnitude, unless the galaxy redshifts are known and a bolometric correction is made. Since such a correction must include knowledge of each galaxy's spectral energy distribution, an iterative approach is required. For this reason, isophotal photometry is not considered further.[5] The other schemes all have their merit, particularly because they are designed to measure a fixed fraction of a galaxy's light regardless of redshift. For practical reasons we adopt the method of Kron for two of our fields (SA68 and SA57), since two-thirds of the optical photometry used here is based on catalogues produced by Kron (1980) and Koo (1986). This method employs an aperture with radius equal to twice the first radial moment of the light profile, denoted as $2r_1$. Such an aperture provides a compromise between high signal-to-noise and total flux. For our third field, Herc-1, we adopt the 2 arcsec aperture photometry of our existing, optical FOCAS catalogue (Valdes 1982; Munn *et al.* 1993), because the fixed aperture magnitude is the most reliable magnitude available. In order to standardize the photometry, we constructed multiaperture K band photometry to match the optical catalogues, as well as to produce an independent and uniform measure of r_1 and $2r_1$ photometry, as discussed in following subsections.

3.2.2 Potential systematics in $2r_1$ total magnitudes as a function of image structure

Because a field galaxy survey samples a heterogeneous population, it is important to understand not only what fraction of the galaxy light is measured in the photometric aperture, but in particular if there are any dependencies of this fraction on galaxy type or redshift. Neither the $2r_1$ or 2 arcsec apertures will typically enclose all of the galaxy light. However, the $2r_1$ photometry is expected to measure roughly 90% of the light for all types of galaxies at redshifts between 0.1 and 2 (Kron 1980), and 95.6% for a Gaussian light profile. Kron demonstrated that for model exponential disks with 5 kpc ($H_0=50$ km/s/Mpc) scale lengths convolved with a Gaussian point spread function (hereafter PSF) with $\sigma=0.6$ arcsec, the fraction of light enclosed within the *true* $2r_1$ changes by less than 1% over the redshift range $0.1<z<0.5$. For $r^{1/4}$-law spheroids, the fraction of light enclosed at high redshift differs from an exponential disk by 7%. The success of the $2r_1$ aperture to enclose a relatively constant fraction of the total light over a wide range of conditions is due to its dependence on only the light distribution function and not the background or fixed isophotal levels (see definition below). These results are sufficiently encouraging that we can expect to correct reliably the $2r_1$ photometry to considerably better than 10% of true total magnitudes. In fact, this can be done quite naturally using the stellar photometry, as we will describe.

However, we should note that some possible systematics remain with the $2r_1$ photometric scheme for our sample. The above discussion assumed that the true value of r_1 is known, when in fact this quantity is difficult to measure for certain galaxy profiles. The r_1 measure is defined as

$$r_1 \equiv \frac{\int_0^{r_{\max}} rI(r)\,dr}{\int_0^{r_{\max}} I(r)\,dr},$$

where $I(r)$ is the average surface brightness at radius r.[6] It is important to consider the definition of the upper limit of integration ($r_{\max}$) because the measured value r_1 is sensitive to this quantity: if the upper limit is too small, so too will be the measured value of r_1, whereas if the upper limit is too big the accuracy of the measured value of r_1 will be degraded by noise. In the next subsection we compare several different definitions that have been applied to our photometry [Infante (1987) also discusses several methods], but for the discussion at hand we consider the upper limit to be defined recursively as $3r_1(r)$. The advantage of this scheme is that it depends solely on $I(r)$. The choice of the factor 3 was set by simultaneously inspecting model curves of growth for r_1 and the light enclosed by $2r_1(r_{\max})$ for Gaussian and exponential-disk profiles. Less than 2% of the enclosed light

[5]Note that FOCAS total magnitudes, which are based on isophotal magnitudes, have been used in Sec. 2 to define the Herc-1 magnitude-limited sample only, and are *not* used in the subsequent analysis.

[6]Kron defined the lower limit of integration to be 1 in units of pixels of his photographic plate scans, or 0.37 arcsec, but that changing this limit to 0 does not significantly change the result. We assume the growth curve behaves quadratically with r within our smallest aperture.

is lost when the aperture radius is changed from the true $2r_1$ defined in this way.

But r_1 grows extremely slowly as a function of r_{max} for $r^{1/4}$-law light profiles relative to the half-light radius (r_e) and compared to Gaussian or exponential light profiles. Preliminary results from models we have developed to test the effect of changes in intrinsic profile, seeing, and redshift with the above upper limit of integration indicate the measured r_1 for $r^{1/4}$-law profiles will be only 33% of its true value in the low-redshift limit. The flux enclosed in twice this radius is only 62% of total. For galaxies with $r^{1/4}$-law light profiles, once either the redshift has increased or the intrinsic size decreased so that r_e is of order or less than the seeing disk, the enclosed flux within twice the measured r_1 should increase to 80%–90%. At $z=0.1$, a length of 2.5 kpc has an apparent size of 1 arcsec ($H_0=50$, $q_0=0$), which is comparable to the typical seeing disk. Most of the galaxies in our sample which most plausibly are dominated by $r^{1/4}$-law light distributions on the basis of their red colors are at $z\geqslant 0.1$. Therefore, we estimate there may be appreciable systematic underestimates of the total flux (>10%) for only the very few largest spheroidal systems at the lowest redshifts. If we chose a larger value for the r_1 upper integration limit, potential systematics for these few galaxies would be reduced, but the reliability of the measured r_1 for the majority of objects would drop dramatically because of the extra noise added (the current scheme encloses nearly all the light). In other words, we have adopted a compromise between minimizing possible systematic and known random errors. We explore the detailed profile, redshift, and noise dependencies on the measurement of r_1 in a future paper. Infante (1987) has discussed other systematics for the $2r_1$ scheme for galaxy work fainter than this survey.

3.2.3 Application of a standard aperture

The next important consideration is the effect of the somewhat inhomogeneous adopted photometric apertures. Kron (1980) measured r_1 with an upper limit of integration set to a faint, but constant isophote at 1% of sky. Koo (1986) remeasured r_1 in SA68 and modified the algorithm to iterate once: if the upper limit of integration was found to be less than $2r_1$, it was increased by 50%. In our current scheme, mentioned above and tested with the K band photometry, we terminate integration when the upper limit exceeds the current value of $3r_1$. To avoid premature termination due to noise, the upper limit may not be less than 3.75 times the Gaussian σ, which best estimates the core of the image PSF (Kron imposed a fixed, minimum value of 2 arcsec, which is about 3.2 σ for the plates in his study). Our choice of minimum integration limit was influenced by the theoretical consideration that for a Gaussian profile[7], $r_1 = \sqrt{\pi/2}\sigma$, and furthermore σ is a single measure that can be independently defined using bright stars at high signal-to-noise. The values of r_1 determined from K band galaxy images were comparable to the optical values measured by Koo. The dispersion between these two measures was not correlated with color, and therefore plausibly also not with image structure. It is important to note that this result is evidence that there are no strong *apparent* color gradients in our galaxies at radii sufficiently large to perturb the measure of r_1. In contrast, the r_1 values measured with an isophotal upper limit of integration for galaxies in SA57 are systematically smaller than (a) the r_1 values for galaxies of the same magnitude and redshift in SA68 measured using Koo's iterative algorithm, and (b) the r_1 values for the *same* galaxies in SA57 measured in the K band using the iterative algorithm described in Sec. *3.2.2*. However, for stars, the r_1 values in SA57 measured with an isophotal upper limit of integration are accurate, as externally corroborated by independent measures of the PSF by Majewski (1992). These results are consistent with the nature of the change in the r_1 algorithm: by allowing the upper limit of integration to be increased iteratively, the measured r_1 for large extended objects, namely bright galaxies, will be most affected.

In SA57, the effect of systematically smaller apertures for our galaxies was measured to be between 0.18 ± 0.04 and 0.23 ± 0.03 mag, for the median and mean, respectively, where the uncertainties represent the variance between the five bands (*UJFNK*). We determined these values by directly comparing photometry using the optical catalogue $2r_1$ apertures to the $2r_1$ apertures measured in the K band, for each band (the optical multiaperture photometry was extracted from the Rome catalogues discussed in Sec. *2.1*). The ratio of the K band to optical aperture radii is typically 1.4 (because of the different upper limits of integration for the r_1 integral), and the K band $2r_1$ is characteristically around 3.5 arcsec. The consistent result for all bands is yet another check that the effect is not due to some problem with the K band photometry, and another indication that there are no appreciable color gradients between the optical and near-infrared bands at moderate to large radii. There is also no discernible correlation with magnitude for this aperture effect. Finally, this systematic difference is only important for the calculation of total magnitudes. For colors, we simply adopt consistent apertures in all bands (in this case, SA57, the optical catalogue apertures), as described in the next section. When needed, total magnitudes are derived from the K band, $2r_1$ aperture magnitudes and the matched-aperture colors. The photometric errors of the derived optical magnitudes are conservatively set to the quadrature sum of the original optical and K band $2r_1$ magnitude errors. We choose to do this rather than adopt the Rome catalogue photometry because more plates are available in the *U, F*, and *N* bands in the catalogues of Kron and Koo, which significantly decreases the photometric errors of our colors.

The Herc-1 galaxy photometry must also be brought in line with SA57 and SA68. We found that the difference between 2 arcsec and $2r_1$ aperture magnitudes varied substantially with magnitude, although there was considerable scatter even in this correlation, as demonstrated in Fig. 4. The trend and scatter presumably reflect a real trend and dispersion in galaxy size with apparent magnitude. As we have noted before, the difference is typically about 0.3 mag for our sample, where the $2r_1$ apertures include more light. We again made this aperture test for all galaxies in the K band,

[7]There is a typographical error in the sign of the exponent in Kron's (1980) formula relating r_1 to σ for a Gaussian profile.

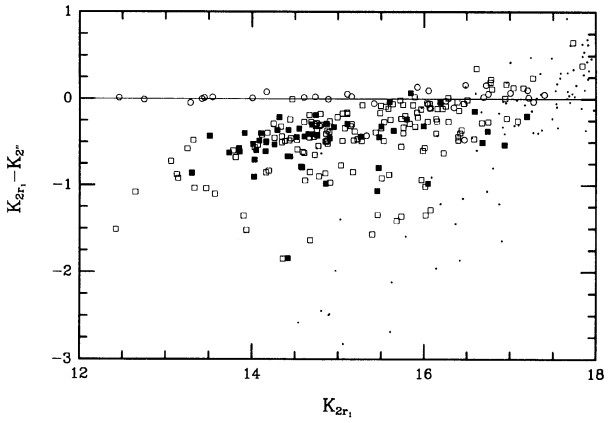

FIG. 4. The difference between fixed aperture and total magnitudes is shown as a function of total magnitude in the K band, where the fixed aperture has a radius of 2 arcsec, and the total magnitude is defined within an aperture of radius $2r_1$ (see text). Open circles represent stars in all fields, boxes represent galaxies in all fields, and dots represent all objects with errors larger than 0.3 mag in either the fixed-aperture or total magnitude. Filled boxes represent galaxies in Herc-1. The line at zero difference is drawn for reference.

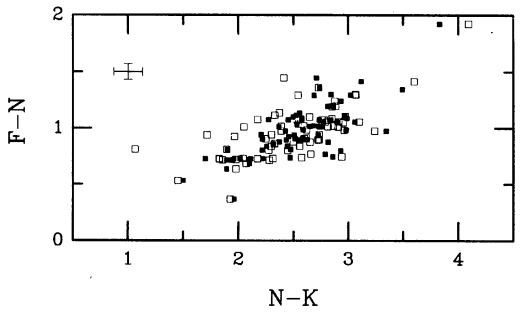

FIG. 5. The photometric effect of determining $2r_1$ on each image is illustrated in the $F-N$ vs $N-K$ two-color diagram. Filled squares are galaxies in SA57 and SA68 that have been photometered using the same aperture in all bands. The open squares are the same galaxies but photometered in the K band using an aperture defined by $2r_1$ in that band.

and for the SA57 galaxies in the optical bands using the Rome catalogues. The scheme to derive total magnitudes in all bands as well as to compute colors is in the same spirit as what we have done in SA57.

3.2.4 Calibration and corrections due to changes in seeing

The last issue involving apertures concerns calibration. Particular attention must be paid to the inherent difficulties of combining photometry from different images and passbands to form colors. For a single image, the zero-point may be set for stellar images with respect to some fixed aperture and, for example, a tertiary, stellar calibration sequence on the image. For extended objects, the zero-point can be set in one of two well-defined ways:

(1) The total flux of the stellar calibrators can be determined for each image via measurements in a fixed aperture and the stellar curve of growth. The latter can be determined to high precision to larger radii with sufficient stars per image, or many images. For example, we are able to determine the stellar curve of growth to 0.5% for the K band survey and the plate data to radii as large as 12 arcsec. The advantage of this first method is that an absolute zero-point is established, which is necessary for calibrating *surface* photometry. However, if the same aperture is used for a given galaxy on a set of images, this will result in a systematic flux decrement as the seeing worsens. One solution is not to use fixed apertures, but to determine, for example, r_1 for each object in each image. Unfortunately, even for galaxies in our survey, which are bright compared to the faintest published galaxy samples, photometry measured within separately determined r_1 for each band results in a substantially larger dispersion in the multicolor distribution than if a single value of r_1 is used for all bands, as illustrated in Fig. 5. We interpret this as significant random error in the determination of r_1. This results in an unacceptable increase in the random photometric error.

(2) Another method is to measure the stellar calibration flux within the same type of aperture used for the galaxies, which in our case is either $2r_1$ (where r_1 for the calibration stars is the stellar r_1) or 2 arcsec. If comparable fractions of the total flux are enclosed for stars and galaxies, the resulting calibration will yield total galaxy magnitudes. To first order, different seeing conditions will affect the amount of light for stars and galaxies the same way, provided the apertures are reasonably matched to the characteristic scale of each object's profile. At a radius of $2r_1$, the curve of growth is fairly flat and at nearly the same level for all profile types. Moderate changes in seeing will therefore cause minor perturbations to the relative values of the curves of growth between objects with different intrinsic profiles. This is effectively how the existing catalogue galaxy photometry was calibrated.

For the Herc-1 photometry, in particular, it is important to test whether such a calibration scheme really works, and that it removes the effects of seeing, since 2 arcsec apertures are significantly smaller than the galaxy $2r_1$ radii. We now proceed to demonstrate the success of this technique using the K band data for the four types of photometric apertures in this survey:

(i) "Near-infrared $2r_1$" radius apertures, where r_1 is measured using an iterative upper limit of integration set to $3r_1(r)$ (used for all K band total magnitudes);

(ii) "SA68-optical $2r_1$" radius apertures, where r_1 is measured using an upper limit of integration that is allowed to iterate once by 50% (used for SA68 optical–near-infrared colors);

(iii) "SA57-optical $2r_1$" radius apertures, where r_1 is measured using a fixed, isophotal upper limit of integration (used for SA57 optical–near-infrared colors); and

(iv) 2 arcsec radius apertures (used for Herc-1 optical–near-infrared colors).

First note that most of our images, both in the optical and in the K band, were taken in very uniform seeing, typically between σ=0.45 and 0.6 arcsec seeing. However, the U plates, because of the long exposures and large atmospheric

TABLE 4. Seeing conditions.[a]

Field	U	J	F	N	K[b]
SA68	0.56	0.60	0.61	0.52	0.47±0.19
SA57[c]	0.82 (1.01)	0.62 (0.66)	0.63 (0.53)	0.70 (0.58)	0.56±0.20
Herc-1	0.69	0.61	0.60	0.45	0.59±0.30

Notes to TABLE 4

[a] Seeing is defined as the Gaussian σ in arc seconds for stars, averaged over all observations per band.
[b] The dispersion for the K band is a measure of the variance of the seeing over all observations for objects in each field.
[c] Values in parenthesis are for plates used in Rome catalogues.

refraction, typically have the worst seeing, whereas the *N* plates typically have better than average seeing. The distribution of the measured PSF σ for all the calibration images taken in the *K* band has an anomalously large peak at σ=0.4 arcsec, which corresponds suspiciously to the IRIM plate scale. It is likely that the seeing was often so good that our images were undersampled, and this prevented an accurate determination of the PSF. This is confirmed from visual inspection of the images. However, in what follows, this overestimate does not appear to be important. Table 4 summarizes the seeing conditions for all bands and fields, where no attempt has been made to correct the *K* band numbers for the probable undersampling of the PSF.

In Fig. 6, the difference between *K* band galaxy magnitudes measured within the four types of photometric apertures listed above are taken with respect to magnitudes measured in a fixed 8 arcsec radius aperture, and plotted versus the estimated PSF. Since the typical value of $2r_1$ is about 3.5 arcsec for our galaxies, an 8 arcsec radial aperture magnitude is a true total, albeit noisy magnitude. These differences are shown in the left panels for photometry using zero-points set to the total flux of the calibration stars [calibration method (1) above]. In the right panels, the differences are shown for photometry using zero-points set to the flux of the calibration stars measured within the appropriate matching apertures [calibration method (2) above].

The magnitude differences using the near-infrared $2r_1$ apertures (top panels of Fig. 6) show little trend with PSF, presumably because the apertures are large and therefore the enclosed flux is little affected by changes in the seeing. However, the mean difference shifts from about −0.15 to +0.05 mag between left and right panels. Hence a 15% systematic error in the estimate of the total flux has been decreased threefold by adopting the second method of calibration. In the case of the optical $2r_1$ apertures, galaxies in SA68 and SA57 are marked separately in the middle panels of Fig. 6 to indicate the result of the systematic difference between the two r_1 measures. The SA68-optical $2r_1$ aperture photometry is shifted towards zero difference after the calibration is recalculated using the corresponding stellar $2r_1$ apertures from the *optical* catalogue. The SA57-optical $2r_1$ aperture photometry is also shifted, but still suffers a loss of light on average, as previously discussed. Nonetheless, some of the trend with PSF has also been removed for the SA57 galaxies. Finally, for the 2 arcsec aperture photometry (bottom panels), we consider objects divided into two categories: $1<r_1<2$, and $2<r_1<3$, in units of arcsec. Not surprisingly, the trend in PSF is strongest for galaxies with the smallest r_1. When the calibration is reapplied using 2 arcsec apertures, this correction nicely removes the trend in PSF for the galaxies with smaller r_1, but introduces the opposite trend for the larger galaxies. However, this overcorrection is not large, in particular for the maximum range of PSFs observed for Herc-1 galaxies in all bands, which does not exceed σ=0.75 arcsec.

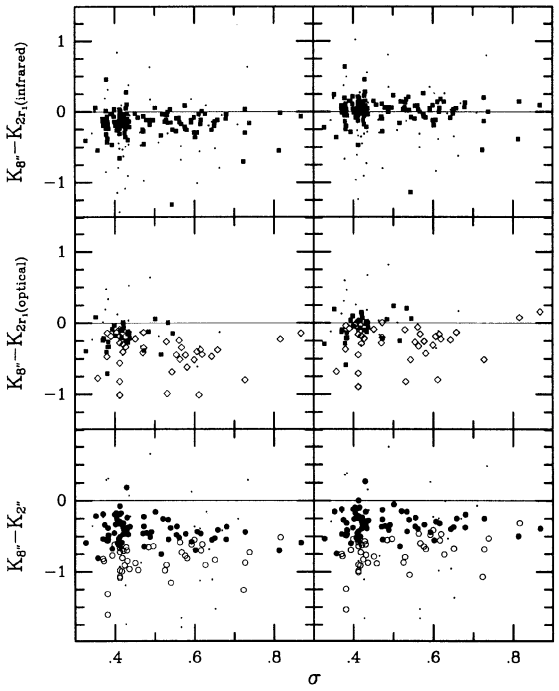

FIG. 6. The photometric effect due to changes in seeing and our calibration scheme is shown for each of the four types of apertures used in our survey. Magnitude differences between a large (8 arcsec radius) aperture and the adopted photometry apertures are shown as a function of the measured PSF (Gaussian σ in arcsec) in the *K* band. The left-hand panels show the photometry calibrated using the total flux of the standard stars. The right-hand panels show the photometry after the calibration has been reset using stellar apertures matched to the galaxy photometry (see text). In the top panel all galaxies are shown using near-infrared $2r_1$ apertures. The middle panel contains galaxies in SA57 (open diamonds) and SA68 (filled squares) using the SA57- and SA68-optical $2r_1$ apertures, respectively. The bottom panel includes all galaxies using a fixed aperture, 2 arcsec in radius. Open circles are galaxies with $2<r_1<3$ and filled circles have $1<r_1<2$ (arcsec). Dots in all panels represent galaxies with 8 arcsec aperture magnitude errors >0.4 mag. Lines have been drawn at zero difference for reference.

There are three final items of note: (1) The PSF was determined for the near-infrared images by interpolating between sets of calibration images. The uncertainty in this interpolation is not expected to be large, with typical errors of about 10%–20% in the determination of the PSF σ. The uncertainty is small because we calibrated frequently, often measuring nearby bright stars simply to determine the PSF. In addition, the PSF in the *K* band was typically very stable in time except at the beginning of the night. The expected error in the PSF determination was propagated through to the adopted zero-point errors, and onwards to the final magnitude errors of the galaxy photometry. (2) In the case where we have used the Rome catalogues for the 15 bright galaxies in SA57, we adopt the near-infrared $2r_1$ aperture, and correct the plate calibration accordingly. (3) We note that the shape

of the PSF does *not* appear to be the same in all bands at large radii. The PSF in the K band appears to be more extended than the optical PSF as compiled by King (1971) beyond radii of 3 arcsec. Our averaged stellar profiles extend to as much as 10 arcsec in radius at high signal-to-noise. This result has been qualitatively confirmed by a comparison to the stellar growth curves as a function of the core PSF on the photographic plates. Both optical and infrared PSFs have significant, though different, non-Gaussian wings. The effects on the multiband galaxy photometry due to differences in the PSF should naturally be removed by our calibration scheme, in particular in the case when $2r_1$ apertures are used. If anything, the extended wings of the star profiles make them more like galaxies, which should enhance the accuracy of this technique.

3.2.5 Potential systematics in the integrated colors due to finite apertures

Gradients in stellar populations, dust, and gaseous emission will in principle produce color gradients in galaxies. Simply put, bulges of spiral galaxies are optically redder than disks, and therefore one expects that optical colors measured in successively larger apertures will become progressively bluer. For a sample of galaxies observed over a large range of distance, and hence apparent size, it is therefore conceivable that systematics will be present in the measured colors as a function of redshift *if* the photometric algorithm does not compensate for this change of apparent size, e.g., if an aperture of fixed size is used. The presence and amplitude of such distance-dependent systematics become increasingly important to understand if colors are to be used to measure galaxy evolution, or if color is to be correlated with luminosity. In the latter case distance-dependent systematics are important because in magnitude-limited samples the most luminous galaxies will tend to be found at the largest distances, while the least luminous galaxies will be found at the smallest distances. Since we intend to do such analyses in future papers, this section briefly reviews what is known about the amplitude of color gradients in galaxies based on studies of nearby galaxies.[8] We then derive the expected effect of color gradients on the measured colors as a function of redshift and absolute magnitude for our galaxy sample and photometric algorithms. Since our photometry is largely based on total magnitudes, we expect the effects of color gradients on the integrated colors of our sample to be negligible. We proceed to establish this initial expectation.

For clarity, it is useful here to compile information on color gradients in simply two colors, $U-V$ and $V-K$, that span the effective wavelength of our data set. The definitive work on *UBV* radial color gradients for galaxies of all types has been established by de Vaucouleurs (1961) and de Vaucouleurs *et al.* (1976, hereafter referred to as RC2). Huchra's (1977) multiaperture photometry of Markarian galaxies compares favorably to the mean color–aperture curves of RC2. His study also extends color–aperture relations to $V-R$, which shows smaller gradients than in $U-B$ or $B-V$. Unfortunately there is no detailed study of near-infrared gradients for all galaxy types that is in any way comparable to RC2. However, we combine the following several studies which together cover all but the very latest, and presumably bluest, galaxies: $V-K$ color–aperture relations for early-type galaxies (Hubble-type E and S0) from Grasdalen (1975) and Frogel *et al.* (1978); Griersmith *et al.* (1982) for early-type spirals (Hubble-type S0 to Sb); and Frogel (1985) for the inner parts of late-type spirals (Hubble-type Sb to Sd). The last two studies derive both $U-V$ as well as $V-K$ color–aperture relations.

To get a sense of the characteristic amplitudes of the color gradients that are relevant to our photometry, we explore the change in color [Δ(color)] between the total and half-light radii. From RC2 we find $0.03<|\Delta(U-V)|<0.17$ [except for types later than spirals $\Delta(U-V)$ is positive]. Hubble-type Sb galaxies have the largest gradients whereas earlier- and later-type galaxies have the smallest gradients. This is not unexpected since Hubble-type Sb galaxies, which are of intermediate color, have both prominent bulges as well as star formation in their disks.

In contrast to the $U-V$ color–aperture dependence on galaxy type, Griersmith *et al.* find that there is little type-dependence to the slope of the $V-K$ color–aperture relation, in agreement with Aaronson (1977).[9] Combining the ratios of the slopes of the color–aperture relations, $U-V:V-K$, for E/S0 (Frogel *et al.* 1978) and late-type spirals (Frogel 1985) with the $U-V$ color–aperture relations from RC2, it appears that all galaxies at least as late as Hubble-type Sd have small, and relatively constant $V-K$ color gradients. The change in integrated color between the total and half-light radii is of order 0.05–0.07 mag.

To estimate how the above gradients affect our photometry, first note our $2r_1$ photometric algorithm employs a metric aperture in the sense that identical galaxies observed at different distances have apparent r_1 that scale only by the inverse of the distance. The beauty of this approach is that identical galaxies are sampled similarly at all redshifts. Next recall that an aperture of size $2r_1$ samples roughly 90% of the total light of a galaxy (modulo systematics for well-resolved $r^{1/4}$-law profiles discussed in Sec. *3.2.2*). Then from the results of RC2, the $U-V$ color–aperture correction to the integrated, $U-V$ color is of order 0.02–0.03 mag, which is negligible for our purposes. The correction for $V-K$ is even smaller. Moreover, *all* colors measured within an aperture of radius $2r_1$ will have this same correction, so there will be no distance dependence to the colors, again modulo the potential systematics discussed in Sec. *3.2.2*. Such potential systematics are only for $r^{1/4}$-law profile dominated systems, which will have small color gradients.

However, we noted in Sec. *3.2.3* that the optical values of

[8]Here we use traditional, Hubble-type morphological labels since this is the framework within which local galaxy studies have been undertaken and within which color-gradient data have been binned. We use the results of de Vaucouleurs (1961) and Huchra (1977) to infer average color types from morphological types.

[9]Griersmith *et al.*'s $U-V$ color–aperture gradients agree with RC2, assuming that magnitudes within an isophote of 25 mag arcsec^{-2} (B) are nearly total, and extrapolating Griersmith's color–aperture regressions from a $\log(A/D)$ value of -0.2 to 0., where A is the aperture diameter and D is the diameter at the above isophote.

r_1 for galaxies in SA57 appeared to be systematically too small compared to our near-infrared measures. The result was a difference of about 0.2 mag between measured and total magnitudes (in the optical). Again using the above results, corrections to $U-V$ will be less than 4%, and 1%–2% for $V-K$. Most galaxies (i.e., all but intermediate types) will have substantially smaller, and therefore insignificant $U-V$ corrections.

A potentially more dramatic color-gradient effect might be expected for one-third of the sample, namely galaxies in Herc-1. Their 2 arcsec aperture photometry samples significantly less than the total light, as illustrated in Fig. 4. However, for all but eight of these galaxies, the fixed aperture encloses *more* than half the light, and so the effects of color gradients on the measured colors is small to moderate (<10%–15% for $U-V$). We make no color–aperture corrections to our measured galaxy colors, even for the eight mentioned above, because (1) for most Herc-1 galaxies the $U-V$ correction will be much less than 10%–15%, and the $V-K$ correction even smaller, (2) there is a large scatter in the color–aperture relations as seen in Griersmith *et al.* (1982) or RC2, comparable to the magnitude of the correction, (3) the correction has been established as a function of morphological type and such types cannot be reliably established for galaxies in our sample because of their great distance (see Sec. 4). Since only galaxies in Herc-1 are affected, we can inspect whether these galaxies display systematically different colors relative to galaxies in the other two fields. Indeed, such checks, presented in Sec. 5, show no systematic color differences between samples in different fields.

Because we will be studying the correlation of color to luminosity as a function of galaxy type in paper II, we dwell for a moment on further checks of our Herc-1 photometry. In particular, we show that the fixed aperture colors for these galaxies are unlikely to contain distance-dependent biases. The distribution of $K_{2r_1} - K_{2''}$, i.e., the difference between K band total and aperture magnitudes, versus redshift and absolute magnitude are displayed in Figs. 7 and 8 for the magnitude-limited sample defined in Table 2(a); the mean and median values for this magnitude difference are tabulated in Tables 5(a) and 5(b). The sample considered here has been restricted to include only objects with secure redshifts and K band photometry with a precision better than 20%. Although a weak dependence on redshift can be seen, there is almost *no* dependence on K absolute magnitude [defined in Table 5(b)] (there is also no dependence on optical absolute magnitude). The reason for this is actually not surprising since in a magnitude-limited sample, more luminous galaxies are seen at preferentially larger distances (a reflection of the shape of the luminosity function and the increase in survey volume at higher redshifts), and more luminous galaxies tend to be larger (e.g., Huchra 1977). These two effects tend to cancel so that the mean *apparent* size of galaxies in magnitude-limited samples is not a strong function of distance or absolute magnitude.

In conclusion, between redshifts of 0.01 to 0.3, our sample at most suffers from color-gradient induced color systematics of order 5%, but again only for blue-optical colors of intermediate-type galaxies in one-third of the sample.

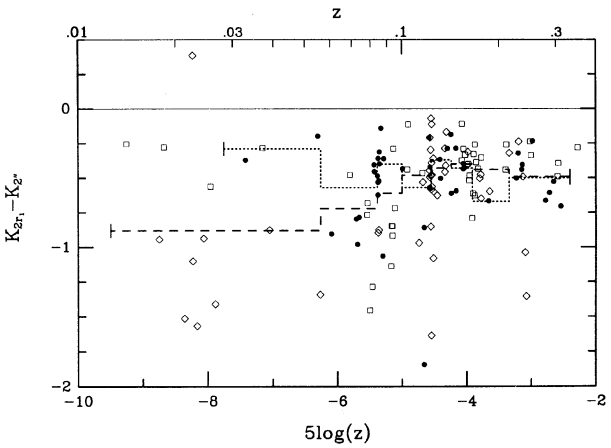

FIG. 7. The difference between total and fixed aperture magnitudes in the K band is shown as a function of redshift. Magnitudes are defined as in Fig. 4. Only galaxies in the J magnitude-limited sample [Table 2(a)] with definite spectroscopic redshifts and photometric errors in both apertures less than 20% (each) are displayed. Diamonds represent galaxies in SA57; boxes represent galaxies in SA68; and filled circles represent galaxies in Herc-1. Dashed and dotted lines represent median values of magnitude differences as tabulated in Table 5(a) for all galaxies and Herc 1 galaxies, respectively. Solid line at magnitude difference of zero is drawn for reference.

For most of this one-third, systematics are expected to be much less than 5%. For the other two-thirds of our sample such systematics are completely negligible to within the photometric precision. Optical–near-infrared gradients for all galaxies are expected to be smaller than a few percent. From this analysis we also conclude that studies of the correlation of color with luminosity and/or redshift will suffer from no significant bias due to color gradients and our adopted photometric procedure.

3.2.6 Summary of the photometric procedure

In summary, the fraction of light measured for galaxies in SA68 in all bands and for *all* galaxies in the K band is

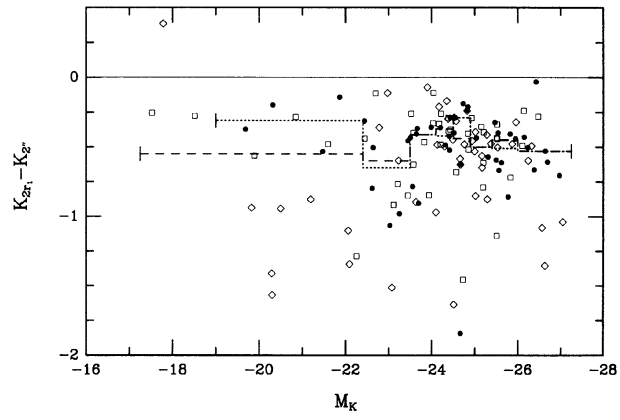

FIG. 8. The difference between total and fixed aperture magnitudes in the K band is shown as a function of total, K band absolute magnitude. Sample, symbols, and lines are as in Fig. 7; median values are tabulated in Table 5(b).

TABLE 5(a). $K_{2r_1}-K_{2''}$ vs redshift.

		All Fields				Herc-1			
Δz		$<>$	σ	median	N	$<>$	σ	median	N
0.000	0.056	−0.75	0.58	−0.88	15	−0.29	0.12	−0.29	2
0.056	0.084	−0.74	0.31	−0.72	16	−0.63	0.21	−0.57	10
0.084	0.100	−0.63	0.32	−0.61	14	−0.46	0.29	−0.40	7
0.100	0.123	−0.59	0.45	−0.48	21	−0.78	0.64	−0.57	5
0.123	0.142	−0.44	0.23	−0.43	16	−0.39	0.17	−0.37	5
0.142	0.165	−0.41	0.15	−0.40	15	−0.43	0.11	−0.43	5
0.165	0.215	−0.46	0.14	−0.44	15	−0.67	···	−0.67	1
0.215	0.310	−0.53	0.29	−0.49	17	−0.49	0.16	−0.50	9

TABLE 5(b). $K_{2r_1} - K_{2''}$ vs absolute magnitude.[a]

		All Fields				Herc-1			
ΔM_K		$<>$	σ	median	N	$<>$	σ	median	N
−27.1	−26.0	−0.60	0.34	−0.53	15	−0.50	0.23	−0.53	7
−26.0	−25.4	−0.54	0.22	−0.45	16	−0.54	0.18	−0.51	8
−25.4	−24.9	−0.54	0.18	−0.50	16	−0.50	0.10	−0.50	2
−24.9	−24.5	−0.61	0.50	−0.44	18	−0.54	0.59	−0.29	7
−24.5	−24.1	−0.40	0.18	−0.37	18	−0.42	0.09	−0.42	5
−24.1	−23.5	−0.48	0.27	−0.41	15	−0.54	0.24	−0.41	6
−23.5	−22.4	−0.65	0.38	−0.60	15	−0.69	0.31	−0.65	6
−22.4	−17.5	−0.68	0.53	−0.55	18	−0.31	0.18	−0.31	4

Notes to TABLE 5(b)

[a]The absolute magnitude is calculated in the K band using the formula $M_K=K_{2r_1}-5\log(d_l/h)+2.5(1+\alpha)\log(1+z)-42.38$, where d_l is the dimensionless luminosity distance $\{d_l=[q_0z+(q_0-1)(\sqrt{1+2q_0z}-1)]/q_0^2$ if the deacceleration parameter $q_0>0$ and the cosmological constant $\Lambda_0=0\}$, $h=H_0/100$ km s^{-1} Mpc^{-1}, and α is the spectral index assuming a power law of the form $f_\nu=\nu^\alpha$. We adopt $h=0.5$, $q_0=0.1$, $\Lambda_0=0$, and $\alpha=1.25$. The latter quantity, which is part of the κ-correction term in the equation for M_K, is justified in Paper II.

expected to be near 90%. The final, calibrated photometry should be very nearly total magnitudes since the calibration corrects for missed light. For SA57 and Herc-1, the fraction of measured light in the optical bands is typically somewhat smaller (60%–70%). Colors are always determined within matching apertures, and our calibration technique corrects for most of the effects due to changes in seeing. We expect that systematics introduced by seeing changes in our galaxy colors are considerably less than 5%. We expect systematics introduced by color gradients in our galaxy colors also to be much less than 5%. Twice the radial moment r_1 introduced by Kron (1980) provides an optimum aperture which includes most of the flux, is large enough to be weakly affected by seeing, but is not too big to compromise the signal-to-noise.

3.3 Photometric Zero-Points

The absolute calibration of our K band photometry and photographic optical photometry is described here. We construct our best estimate for the K band response function of the IRIM. We then use this function along with previously estimated response functions for the *U, J, F,* and *N* bands to demonstrate that our calibrated stellar photometry agrees with the spectral library constructed and compiled by Persson (1987) and Bruzual (Bruzual & Charlot 1993, hereafter BC93; Bruzual 1992). This library, which we use extensively in Paper II, consists of the stellar spectrophotometry of Gunn & Stryker (1983) and Strecker *et al.* (1979, 1989), and its construction is described in detail in BC93. The zero-point for the K band is set to the CIT near-infrared system (Elias *et al.* 1982) as discussed in Sec. *3.1.3*. The principal purpose of this section is to establish the absolute calibration between the optical and near-infrared photometry in the linear regime of the photographic plates. Further demonstrations of the absolute photometric calibration at bright, optical magnitudes and comparisons between fields for both galaxies and stars are presented in Secs. *3.4* and 5.

3.3.1 Optical zero-points

The zero-points for the optical photometry have been set by Kron (1980) for the *J* and *F* bands in SA57 and SA68 using existing *B* and *V* band photoelectric photometry for stars and galaxies in these fields, compiled from several sources (see discussion in Majewski 1992). Koo (1986) established the zero-points in the *U* and *N* bands using a variety of techniques, namely applying expected relations between *N, B,* and *V* bands for the photoelectric standards, determining the position of a sharp bend in the stellar locus in the $J-F$, $F-N$ two-color plane, and matching colors of galaxies to the predictions of Bruzual's models (1981). For the *U* band, Koo was also able to test directly the relation between the photographic and photoelectric systems in a different field (SA 99). The more recent *UBVRI* CCD images in subfields of SA57 and Herc-1 obtained by Majewski, Koo, and Kron (in preparation) were used in SA57 by Majewski (1992) to calibrate further the *U, J,* and *F* bands, as well as set a preliminary zero-point for the *J* and *F* bands in Herc-1. The *U* and *N* band zero-points in Herc-1 were set in the same manner as Koo set these zero-points in SA57 and SA68.

Here, we utilize more recent reductions of the same CCD photometry in SA57 and Herc-1 to revisit the calibration of the optical catalogues. In particular, we now are able to calibrate the *U* and *N* bands directly from the tertiary standards established by the CCD photometry, and we do not have to appeal to more indirect techniques. We find that the resulting changes to the existing zero-points are very small, resulting in color changes of at most 0.03 and 0.11 mag in SA57 and Herc-1, respectively. This is reassuring in light of the fact we have no new calibration for the SA68 field.

The two critical steps in setting our galaxy catalogue zero-points are (1) determining the magnitude at which stars are no longer saturated, and (2) determining the transformations between the standard systems and our photographic system. Transformations between the standard *UBV* system and the Kron–Cousins *RI* system of the CCD photometry to the *U, J, F,* and *N* photographic system are from Majewski (1992) [see Table 4 of Majewski (1992) for references to the standard systems]. After tertiary standards were rejected for saturation, contamination due to nearby objects, extreme colors outside the range of the airmass correction equations, identification as galaxies or QSOs, or extreme deviance, the following number of stars remained: in SA57 there were 8, 28, 30, and 16 stars in the *U, J, F,* and *N* bands, respectively,

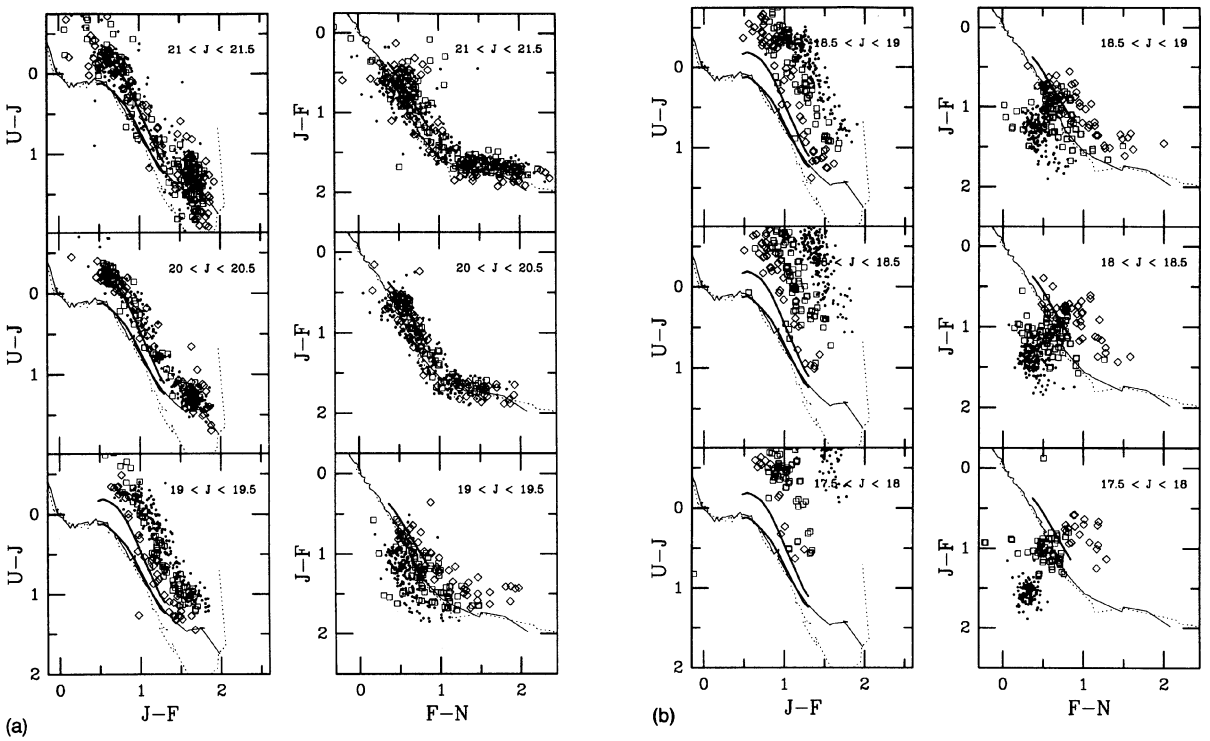

FIG. 9. Two-color diagrams for $U-J$ vs $J-F$ and $J-F$ vs $F-N$ for stellar objects as a function of J magnitude: diamonds (SA57), boxes (SA68), and small, filled circles (Herc-1). Trends with magnitude largely reveal effects of photographic saturation, whereas colors at the faintest magnitudes demonstrate the accuracy of the photometric calibration. Zero-points have been applied for each band and field, as described in the text. Objects are binned in half-magnitude intervals spanning $19<J<21.5$ (a), and $17.5<J<19$ (b). The thin, solid curve represents the solar-metallicity stellar main sequence, as defined by the catalogue described in the text (and Bruzual & Charlot 1993). The thin, dashed curve is for near-solar-metallicity giants, from the same catalogue. Note the upturn in $U-J$ for giants at red $J-F$ is consistent with the behavior of late-type giants in *UBV* colors as tabulated by Johnson (1966). The thick, solid curves in $U-J$ vs $J-F$ plots are adopted from Majewski (1992, Fig. 6, and references therein), and represent the locus of Hyades main-sequence stars (lower left) and the limit for extremely metal-poor stars (upper right). The thick, solid curve in the $J-F$ vs $F-N$ plots represents a portion of the metal-poor main sequence ($0.5<\mathcal{M}/\mathcal{M}_{\odot}<1.0$, $Z=0.0001$, $Y=0.20$) from the models of Vandenberg & Bell (1985). *JFN* colors are determined from the *BVRI* model colors and the transformations of Majewski (1992).

and in Herc-1 these respective numbers are 8, 5, 7, and 6 stars. We estimate that errors in this calibration are less than 5% in all bands.

To illustrate the relative and absolute calibration of our optical colors, the two-color plots for $U-J$ vs $J-F$ and $J-F$ vs $F-N$ are displayed in Fig. 9 for stars. At bright apparent magnitudes ($J<20-19.5$), the stellar colors change rapidly as a function of apparent magnitude and field. Such behavior indicates the onset of photographic saturation. At fainter magnitudes ($J>20$), the stellar photometry is stable, i.e., the position (colors) of the stellar locus does not change with apparent magnitude. Note that only stars typically fainter than $J=20$ were used to establish the photometric zero-point. Moreover, the position of the stellar locus is the same (to within 5%) for all fields (relative color calibration), and matches the predicted colors for galactic stars covering a range of metallicity expected for galactic disk and halo stars (absolute color calibration). The reliability of photographic photometry for faint objects ($J>20$) on our 4 m photographic plates has also been confirmed to be within the estimated photometric accuracy via direct comparison to other CCD-calibrated photographic photometry for the J and F bands (Infante & Pritchet 1992), and for the F and N bands utilizing the CCD data of Hall & Mackay (1984).

3.3.2 The IRIM K band response function

The response function for the KPNO IRIM was determined from tracings of the K band filter used during our observations and the KPNO summer atmosphere model of Manduca & Bell (1979). We have neglected any spectral dependence of the InSb device because such devices are known to have nearly uniform response across the K bandpass. Two identical K filters (Optical Coating Laboratory, Inc., United Kingdom) were used together to suppress any possible red leak. Tracings were kindly provided by Probst (1992), and R. Bell kindly made his models available in computer readable format. The summer KPNO model was adopted because for a similar K band filter (Manduca & Bell 1979) this atmosphere yielded the identical airmass extinction coefficient between 1 and 2 airmasses as we observed at KPNO over our four runs (0.07 ± 0.01 mag per airmass). Our simulated transmission functions at 1, 1.15, and 2 airmasses represent the low, characteristic, and high airmasses of our observations. These functions, along with the model atmosphere, are shown in Fig. 10 at a resolution of 0.1%. We adopt the curve at 1.15 airmasses for the remainder of this work.

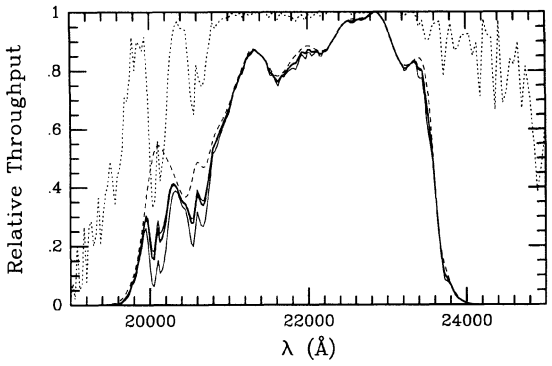

FIG. 10. *K* band response function for the KPNO IRIM as constructed in this work (see text), and atmospheric extinction (Manduca & Bell 1979) are plotted vs wavelength. The heavy solid line is the adopted curve using 1.15 airmasses of atmospheric extinction. Light solid lines represent models using 1 and 2 airmasses; the dashed line is the product of the filter transmission alone; and the dotted line is the model atmospheric transmission at 1 airmass for KPNO in the summer.

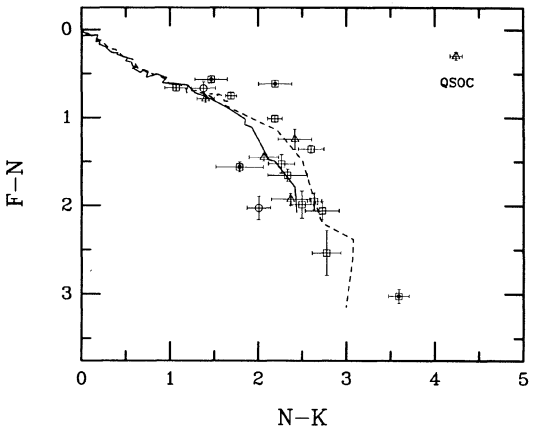

FIG. 11. $F-N$ vs $N-K$ for 21 stellar objects with color errors <0.3 mag. The solid and dashed lines represent main sequence and giant stars, respectively, in the Bruzual–Persson/Gunn–Stryker library used in Bruzual & Charlot (1993). Stars are from our three fields: Herc-1 (boxes); SA57 (circles); and SA68 (triangles). Dotted objects were observed with PNIC. The object labeled "QSOC" has been previously selected as a QSO candidate on the basis of its optical colors (Kron *et al.* 1991).

3.3.3 Test of the optical–infrared color zero-point

A moderate number of galactic stars were serendipitously imaged in our *K* band survey. Of these, 21 are not saturated on the plates, and yet have photometric errors small enough (<0.3 mag in the colors) to be useful for comparison with the stellar colors of the spectral library introduced above. Here we compare the colors of the stellar locus predicted from this library and the *F*, *N*, and *K* transmission functions to the observed stellar $F-N$ vs $N-K$ colors, as displayed in Fig. 11.[10] The agreement is remarkably good, and is a confirmation both of our photometric calibration, the adopted transmission functions, as well as the careful calibration and compilation of the spectral library by Persson and Bruzual. If we adopt the *K* band filter function of the CIT system (as tabulated in Bruzual's models), the stellar locus changes by less than 3%, and only for $F-N$ redder than 2.25. Hence our *K* band is very close to this standard system.

Finally, the few deviant points are worthy of mention. Four objects doubly marked with solid dots in Fig. 11 represent *K* band observations using PNIC. Although these points don't agree with the predicted colors to within the estimated errors, there is no systematic color offset. The deviance may be indicative of an underestimate of the errors for the data from this camera. Observations using this camera are flagged in the following analysis. The one star in SA57 near $F-N=2$ and $N-K=2$ which lies far from the stellar locus was observed on three separate occasions, and the measures were in agreement within the quoted errors. Therefore, we do not have a plausible observational explanation for its colors. The one object with extreme colors, both blue in $F-N$ and red in $N-K$, was previously selected in the optical bands to be a QSO candidate (Kron *et al.* 1991).

[10]The colors derived from the library were calibrated using the Vega model of Kurucz (1979), interpolated by Bruzual (1992) beyond 1.8 μm using a black body of 9400 K. Only the 103 stars from the library used in BC93 are used, out of a total of 175 stars in Gunn & Stryker (1983). As noted in BC93, these 103 stars were selected to have solar-metallicity colors. In practice this excludes the two latest types for both dwarfs and giants, all carbon stars, and supergiants from Gunn & Stryker. However, the remaining 103 stars go as late as M6 V and M6 III.

3.4 Photographic Saturation

Photographic photometry suffers from emulsion saturation for objects at bright magnitudes. This is particularly a problem for stars, due to their compact light profiles, although the problem can be surmounted successfully by using profile fitting photometric techniques (e.g., Stetson 1979), as demonstrated by Majewski using some of the same plates in this study. A similar solution cannot be employed for galaxies because of their *a priori* unknown and varied light profiles. On the other hand, because galaxies tend to have more diffuse light profiles than stars, one expects their photographic images to remain unsaturated to brighter integrated magnitudes than for stars. Because we are without CCD photometry for most bands and fields, we must estimate and correct for photographic saturation effects in galaxies via the several dozen photoelectric and CCD standard stars in each of our fields used in Sec. 3, as we describe below. We first discuss several tests to determine at what magnitude galaxy images begin to saturate significantly on the photographic emulsion relative to stars, as a consistency check of our expectations. We proceed to describe a method of correction and quantify the magnitude of the saturation effect for stars and then galaxies.

3.4.1 The onset of saturation

The multicolor distribution of objects, when compared for adjacent bins in apparent magnitude, reveals the onset of saturation because the degree and rate of saturation is invariably different in different bands (i.e., on different plates). When saturation occurs for stars, this causes a rapid shift in the position of the stellar locus, as illustrated in Fig. 9 between $19<J<20$. The onset of saturation occurs roughly

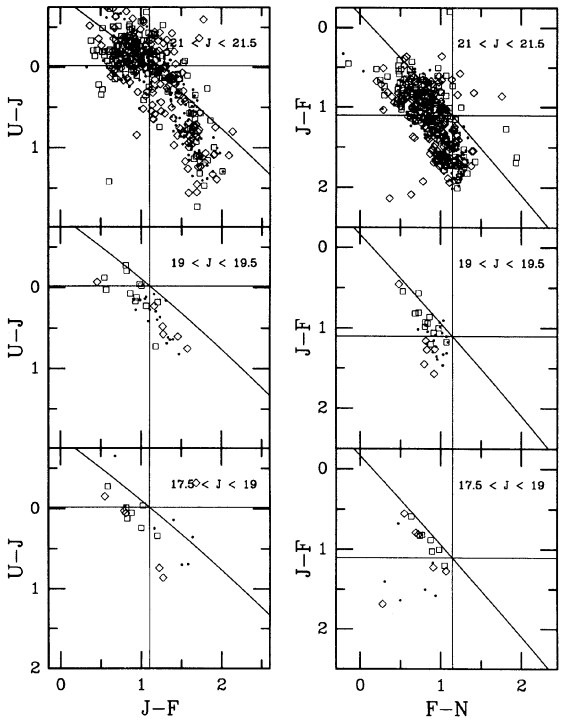

FIG. 12. Two-color diagrams for $U-J$ vs $J-F$ and $J-F$ vs $F-N$ for extended objects (galaxies) as a function of J magnitude. Objects are marked differently for each of three fields: SA57 (diamonds), SA68 (squares), Herc-1 (small, filled circles). Trends with magnitude are to be compared to Fig. 9 for stellar objects. Zero-points have been applied for each band and field, as described in the text. Objects are binned in three magnitude intervals spanning the range of Figs. 9(a) and 9(b), namely $17.5 < J < 21.5$. The decreased resolution in magnitude at brighter magnitudes compared to Fig. 9 is to compensate for the paucity of bright galaxies relative to stars. The diagonal curves in both left and right panels represent the colors corresponding to a single power-law spectrum (i.e., constant α, where $f_\nu \propto \nu^\alpha$) over the observed wavelength range spanned by *U, J, F* and *J, F, N* bands, respectively. Cross-hairs intersect the power-law curve at index $\alpha = -3.0$. These sets of curves are for reference.

around $J=19.5$ for stars in all three fields, although the amount of saturation for each band is indeterminate from these plots alone. The effect for galaxies appears to be more gradual, as illustrated in Fig. 12, and as expected given the variety and greater diffuseness of galaxy profiles. The appearance of such an effect for galaxies is also somewhat complicated by changes in characteristic redshift (and hence color) with apparent magnitude. Nonetheless, one can assess that significant saturation for the majority of galaxies does not occur until $J<18.5$, or about one magnitude brighter than for stars.

Another clear indication of saturation for stars is the sudden and sharp apparent increase in r_1 (e.g., Kron 1980, Fig. 9) at bright magnitudes. One would expect a similar phenomenon to occur for galaxies as their images become saturated, although such behavior will be complicated by the fact that bright galaxies will systematically be at lower redshifts and hence have larger apparent sizes. However, because the K band measures of r_1 do not suffer from saturation, a differential comparison can be made between the optical and K band r_1 values for both stars and galaxies. Such a comparison will be independent of a galaxy's apparent and intrinsic size. Trends in the ratio of the optical to infrared r_1 are shown in Fig. 13 for the galaxies in the magnitude-limited sample in SA68, and stars in both SA57 and SA68. Note that the r_1 ratios for stars in the two fields have different quantitative behavior as a function of magnitude, which is indicative of different calibration curves at high density, a hallmark of photographic plates. In this case, the onset of saturation happens at fainter magnitudes for SA68 plates than SA57 plates. However, qualitatively, the stellar r_1 ratios both become larger at brighter optical magnitudes, which is consistent with optical saturation, whereas the galaxy r_1 ratios do not increase. From this figure, it can be said conservatively that galaxies fainter than $J=19$ are not saturated significantly.

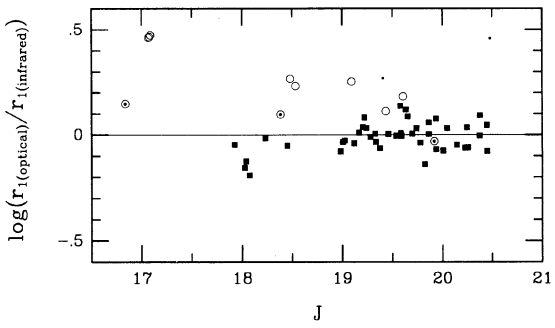

FIG. 13. The onset of photographic saturation is explored for stars and galaxies by plotting the log of the ratio of the infrared r_1 to the optical r_1 vs J magnitude. Stars in SA57 are represented by dotted circles; open circles represent stars in SA68; and boxes represent all galaxies in SA68 in the J magnitude-limited sample.

3.4.2 Saturation corrections for stellar magnitudes

The calibration standards discussed in Sec. *3.3* can be used to directly measure the degree of saturation as a function of stellar magnitude for each band and field. Recall that the zero-points were determined for fainter standard stars that were not saturated. However, there exists a significant number of brighter standards whose photographic photometry is saturated. The difference δm between photographic and CCD (or photoelectric) magnitudes transformed to the same photometric system, minus its asymptotic value at faint magnitudes (i.e., the zero-point offset), gives the saturation correction function $\delta m(m)$ *for objects with stellar profiles*. Applying this correction to the stellar magnitudes results in the multicolor distributions in Fig. 14.[11] Comparison of this figure with Fig. 9 demonstrates the improvement in the stellar photometry at bright magnitudes due to this saturation correction. There is no longer any apparent color offset between fields or with respect to the fiducial loci as a function

[11]For SA68, standard stars were only available for B and V, or J and F photographic bands. Saturation corrections for U and N were determined from the multicolor distributions $U-J$ vs $J-F$ and $J-F$ vs $F-N$, respectively, after J and F bands were corrected, by forcing the stellar loci to agree in the mean with the corrected loci for SA57 and Herc-1.

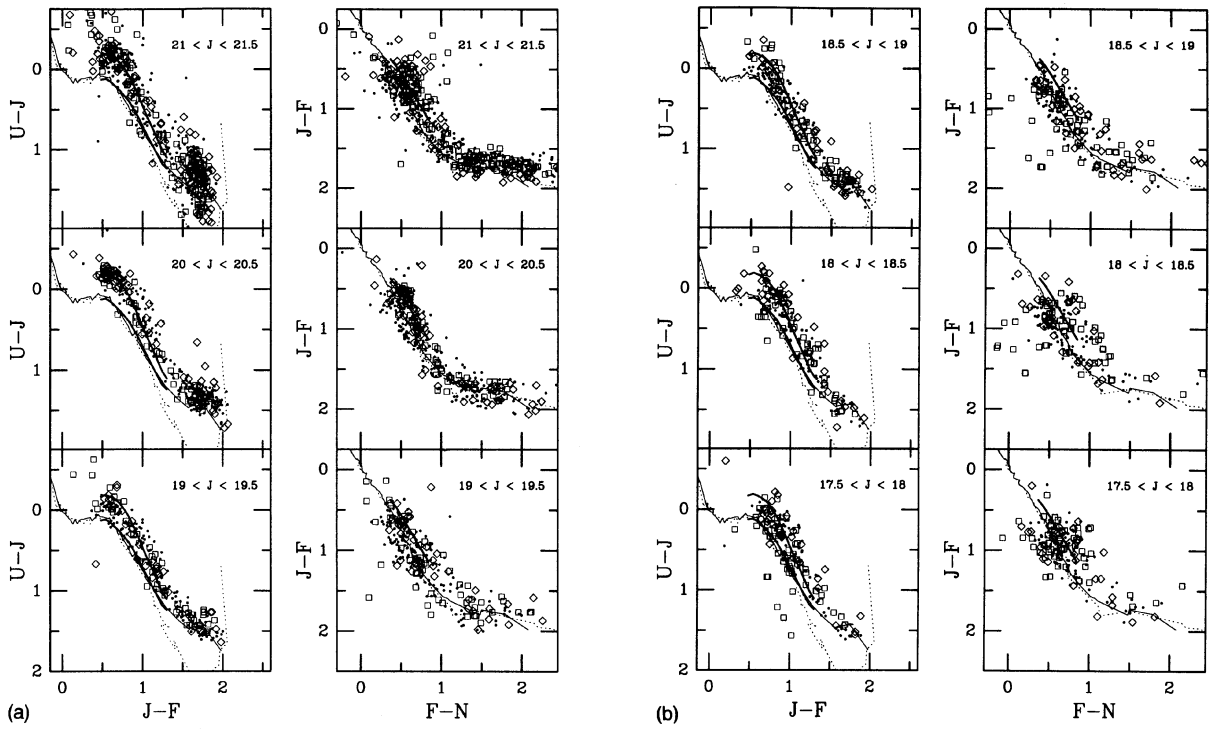

FIG. 14. Two-color diagrams for $U-J$ vs $J-F$ and $J-F$ vs $F-N$ for stellar objects as a function of J magnitude. Binning, curves, and symbols are as in Fig. 9. Zero-points have been applied for each band and field. In addition, stellar magnitudes have been corrected for effects of photographic saturation, as described in the text. Trends with magnitude are to be compared to Fig. 9. The stellar colors now agree in the mean to the predicted stellar colors for a range of metallicity. The trend, seen in $U-J$ vs $J-F$, of finding more stars closer to the near-solar-metallicity main sequence at brighter magnitudes is qualitatively consistent with the results of Majewski (1992), who used a different technique (see text) for photometering stars and handling photographic saturation. This trend is expected if more distant stars are increasingly metal-poor.

of magnitude to within 5% to $J \geq 17.5$. There is, however, an increase in the width of the color distributions at bright magnitude which may be due to an increase in random noise in the photometry due to saturation effects in the photographic emulsion.

3.4.3 Saturation corrections for galaxy magnitudes

To correct galaxy magnitudes for saturation effects we have developed a scheme to relate the well-defined corrections for stars to galaxies of different light profiles and magnitude. This has been done by exploring the emulsion density distributions in both classes of objects. For this purpose and for future studies of galaxy image structure, we have rescanned all survey galaxies as well as a sequence of stars covering a wide magnitude range from heavily saturated to unsaturated (e.g., $17<J<21.5$) in all bands and fields. The details of the plates and scans will be discussed elsewhere, but here it is sufficient to note that galaxy and star scans were done in the same way and at the same time, and that the plates are of comparable quality (if not the same) as the plates used in the catalogues, both in terms of depth and image resolution.

We have measured the peak density as well as the average density within an aperture of radius r_1 (stellar) for all scanned objects (note that r_1 is close to the half-light radius for all profiles, and we find essentially all of the emulsion saturation for stars in the relevant magnitude range occurs within this radius). We then proceeded to define two pseudo-stellar magnitudes (PSM) for each galaxy, namely the magnitude of an object with a stellar profile with the same peak plate density, and alternatively average density, within the stellar r_1 radius. Either of these PSMs can be used to estimate the saturation effect on the galaxy magnitude. More precisely, the saturation correction to the galaxy magnitude is the magnitude correction to the PSM as established from the stellar calibration, but to only that fraction of the galaxy magnitude made up by the PSM.

For the above formalism to be correct, the part of the galaxy profile that is affected by saturation must be stellar. This is not unreasonable since it is largely the unresolved cores of galaxies that constitute the saturated regions, but isn't strictly true since galaxies are less compact than stars. Because of this, the PSM determined from the peak density will tend to *underestimate* the effective saturation because for a given peak density there will be more surface area at higher density in a galaxy image than for the corresponding stellar image. In contrast, however, the PSM determined from the average density within the stellar r_1 will *overestimate* the effective saturation for the same reason: for the same average density, galaxies will have a lower peak density. An average of these two PSM therefore roughly takes into account the nonstellar nature of the galaxy profile in estimating the saturation correction. In addition, the difference between these two saturation correction estimates pro-

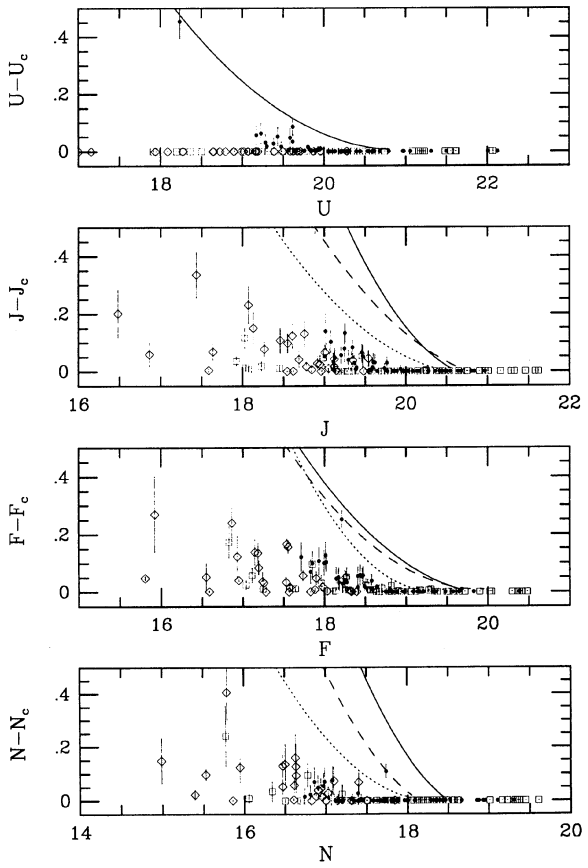

FIG. 15. Saturation corrections (magnitude−corrected magnitude) vs magnitude are displayed for all galaxies in our sample in each of the four photographic bands, *U, J, F,* and *N*. Objects are marked differently for each of three fields: SA57 (diamonds), SA68 (squares), and Herc-1 (filled circles). Uncertainties in the saturation corrections are marked. Saturation corrections for stars are represented as curves: SA57 (dotted), SA68 (dashed), and Herc 1 (solid). The most saturated object in Herc 1 (10292), which falls very near the stellar curves (particularly in *U* and *F*), has a confirmed active nucleus and very compact light profile that is nearly stellar.

vides a reasonable estimate of the uncertainty in the adopted correction. We add this uncertainty in quadrature to the existing estimate of the photometric errors (Koo 1986). This tends to increase the photometric errors for the brightest galaxies. Such a trend agrees qualitatively with the increased width of the *corrected* stellar locus at bright magnitudes in Fig. 14.

In Fig. 15 the derived saturation corrections and correction uncertainties for all objects in our sample are shown for each photographic band as a function of uncorrected magnitude. For reference, the saturation corrections for stars in each field are also shown. The large corrections for the Herc-1 *N* band relative to the other fields is a reflection of the superior seeing on the *N* plates in this field (Table 4). Inspection of Fig. 15 immediately reveals that galaxy saturation corrections are all smaller than corrections for stars at the same integrated magnitude, and moreover very few galaxies have corrections larger than 10%. For the purpose of future analysis and assessment of the photometry, we divide the sample into objects with <5% correction, 5%–10% correction, 10%–20% correction, and >20% correction (in any band). The numbers of such objects are 138, 17, 15, and 6, or 78%, 10%, 9%, and 3%, respectively. We will proceed to show that all but the objects with >20% saturation appear to have reliable photometry to within the photometric errors. This photometric reliability will be established through comparisons of multicolor and color–redshift distributions of our galaxy sample compared to models, as discussed in Sec. 5 and paper II.

Finally, a rigorous but considerably more involved approach to correcting saturation effects has been developed by Kormendy (1973), Nanni *et al.* (1980), and Bunclark & Irwin (1983). However, we have demonstrated that our current approach yields mild saturation corrections for the vast majority of objects. Given the magnitude of the corrections, a more detailed analysis is not likely to change our photometric results by more than a few percent except for the few brightest objects.

3.4.4 Summary of corrections due to photographic saturation

We have shown that accurate corrections for the effects of photographic saturation can be made to stellar magnitudes. Such corrections can be applied to galaxies, once a measure of the effective photographic density in the core of the profile has been made. Saturation corrections for galaxies have been derived from new plate scans of our entire sample. The resulting corrections are small (<10%) for all but 12% of our sample, and the resulting photometric corrections should be accurate to a few percent. For 3% of the objects, saturation is sufficiently large that even the corrected photometry is not reliable; accurate photometry for these objects will require new multiband CCD images. *For the vast majority of objects, saturation is either nonexistent, or reliably corrected.*

3.5 Galactic Extinction

Our three fields were chosen to be in regions at high latitude with low galactic extinction. Galactic reddening estimates for these fields are listed in Table 1. These estimates are very uncertain, as demonstrated by the compilation of Brooks (1981) of discordant reddening predictions from six methods, both stellar and nonstellar. Although it is possible there are appreciable amounts of extinction ($A_V \sim 0.3$) on the basis of Brooks's work, the reddening maps of Burstein & Heiles (1982) using H I column densities and galaxy counts (which Brooks considers) suggest smaller, if not negligible amounts of extinction. In addition, we have no evidence from the distributions of galaxy or quasistellar object colors, nor from the counts, that there are differential effects between our fields, although such differences are suggested by the reddening maps based on *IRAS* 100 μm emission of Boulanger & Perault (1988). However, the resolution of these maps is sufficiently low that we cannot estimate with certainty the reddening values for SA68 and Herc-1 due to the patchy nature of the extinction near these fields. Most estimates are consistent with $E(B-V)=0.02$ mag for all fields. For a standard reddening curve (Johnson 1965), this corresponds to roughly a 10% change in the observed $U-K$ color, namely the longest color baseline of our photometry.

TABLE 6(a). Photometry, apertures, and redshifts for bk and bg spectral-type galaxies.

NSER	Field	α(1950)	δ(1950)	S	K_{total}	U-J	J-F	F-N	N-K	r_1	z	Notes
6589	sa68	0:14:48.55	15:31:57.9	j	17.09 +0.16	-0.28 +0.04	0.56 +0.04	0.37 +0.08	1.96 +0.18	1.28	0.014	
14054	sa68	0:15:40.12	15:43:59.2	j	16.67 +0.14	-0.12 +0.04	0.55 +0.04	0.53 +0.04	1.50 +0.15	1.55	0.018	
13429	sa57	13:05:06.59	29:43:46.4	j	17.84 +0.08	-0.07 +0.04	0.46 +0.04	0.48 +0.11	1.30 +0.14	0.54	0.023	
13976	sa57	13:06:07.60	29:44:38.9	j	15.97 +0.08	-0.13 +0.05	0.53 +0.05	0.55 +0.06	1.63 +0.12	2.44	0.024	
11920	sa68	0:14:48.17	15:40:26.4	j	16.00 +0.09	0.04 +0.05	0.56 +0.05	0.72 +0.04	1.70 +0.12	1.70	0.026	
2097	sa57	13:06:28.37	29:26:08.6	j	15.68 +0.10	-0.04 +0.04	0.61 +0.04	0.51 +0.10	1.80 +0.14	3.72	0.026	
14358	herc1	17:17:44.28	50:06:52.7	j	16.74 +0.12	-0.04 +0.06	0.76 +0.04	0.45 +0.14	1.77 +0.18	1.44	0.033	
2984	herc1	17:19:56.59	49:44:59.3	j	17.19 +0.17	-0.40 +0.05	0.45 +0.04	0.53 +0.07	1.56 +0.17	1.16	0.055	
3848	herc1	17:18:51.15	49:46:44.2	j	15.47 +0.08	0.03 +0.04	0.78 +0.04	0.66 +0.04	1.82 +0.08	2.25	0.072	
17964	herc1	17:18:11.20	50:15:25.1	j	14.57 +0.09	0.42 +0.05	1.22 +0.05	0.77 +0.05	1.99 +0.09	2.15	0.074	
7917	sa68	0:14:12.94	15:34:08.0	j	15.03 +0.07	-0.26 +0.05	0.58 +0.05	0.62 +0.04	1.89 +0.08	2.16	0.078	
14206	sa68	0:14:06.86	15:44:19.6	j	16.07 +0.13	-0.16 +0.04	0.76 +0.04	0.71 +0.05	1.94 +0.14	2.80	0.081	
16752	herc1	17:18:33.19	50:12:26.8	j	16.94 +0.14	-0.09 +0.07	0.66 +0.04	0.52 +0.20	1.84 +0.22	2.07	0.084	
13932	herc1	17:20:18.78	50:05:40.0	j	16.59 +0.11	-0.05 +0.04	0.70 +0.04	0.77 +0.05	1.66 +0.11	1.07	0.086	*K*
8663	herc1	17:20:39.17	49:55:15.4	j	15.45 +0.06	-0.02 +0.05	0.67 +0.04	0.69 +0.09	1.77 +0.11	2.13	0.087	
13504	sa68	0:15:42.38	15:43:01.8	j	18.22 +0.27	-0.11 +0.05	0.58 +0.05	0.58 +0.10	0.33 +1.18	0.63	0.093	
16360	sa68	0:14:21.49	15:48:33.0	j	16.39 +0.09	-0.08 +0.04	0.69 +0.04	0.71 +0.05	1.89 +0.12	1.43	0.104	
13330	sa57	13:06:46.23	29:43:37.5	j	14.91 +0.09	0.03 +0.04	0.79 +0.04	0.69 +0.04	2.14 +0.11	2.72	0.113	
17710	sa68	0:14:50.30	15:51:54.9	j	15.22 +0.07	-0.04 +0.04	0.99 +0.04	0.80 +0.04	2.22 +0.10	1.73	0.116	
19264	sa57	13:06:17.06	29:53:42.8	j	16.22 +0.06	0.00 +0.13	0.66 +0.14	0.61 +0.15	1.78 +0.12	1.39	0.124	*K*
12656	sa57	13:05:30.50	29:42:41.7	j	16.43 +0.10	-0.11 +0.04	0.61 +0.04	0.53 +0.10	1.76 +0.12	1.88	0.125	
12909	sa57	13:05:29.07	29:43:03.0	j	15.98 +0.07	-0.04 +0.04	0.71 +0.04	0.71 +0.08	1.88 +0.11	2.02	0.125	
3536	herc1	17:17:59.47	49:46:14.4	j	16.68 +0.14	0.00 +0.08	0.90 +0.04	0.54 +0.17	1.92 +0.20	1.91	0.132	
9673	herc1	17:18:32.86	49:57:29.4	j	16.04 +0.16	0.15 +0.10	0.99 +0.04	0.72 +0.15	1.91 +0.20	2.76	0.155	*z*1
5799	sa68	0:15:39.87	15:30:42.6	j	16.14 +0.08	-0.03 +0.04	0.80 +0.04	0.72 +0.04	2.09 +0.10	1.53	0.160	
13536	sa68	0:14:15.54	15:43:11.1	j	15.53 +0.07	-0.27 +0.04	0.81 +0.04	0.72 +0.04	2.22 +0.10	1.85	0.162	
9290	sa68	0:14:44.71	15:36:17.9	j	15.76 +0.07	-0.17 +0.05	0.81 +0.06	0.66 +0.05	2.10 +0.09	1.46	0.167	
14712	sa68	0:14:19.71	15:45:16.9	j	16.23 +0.10	-0.13 +0.04	0.74 +0.04	0.73 +0.05	2.11 +0.10	1.61	0.168	
11514	sa68	0:15:16.97	15:39:40.1	j	16.28 +0.09	-0.23 +0.04	0.81 +0.04	0.73 +0.05	2.01 +0.10	1.36	0.168	
6689	sa57	13:05:41.90	29:33:54.4	jz	15.60 +0.03	-0.08 +0.05	0.90 +0.04	0.99 +0.06	2.11 +0.07	1.39	0.230	
13586	sa68	0:15:05.50	15:43:14.1	z	16.61 +0.09	-0.30 +0.05	1.04 +0.04	0.92 +0.05	2.46 +0.13	0.58	0.299	
10585	sa68	0:14:22.06	15:38:16.7	z	16.03 +0.07	-0.27 +0.07	1.36 +0.05	1.02 +0.06	2.68 +0.14	0.93	0.304	
12646	sa68	0:14:49.48	15:41:38.8	z	18.54 +0.16	-0.42 +0.10	1.16 +0.08	0.81 +0.13	2.47 +0.20	0.33	0.304	
10334	sa68	0:14:10.24	15:37:54.8	z	16.02 +0.20	-0.15 +0.06	1.23 +0.04	1.04 +0.05	2.64 +0.31	1.13	0.311	

TABLE 6(b). Photometry, apertures, and redshifts for bm spectral-type galaxies.

NSER	Field	α(1950)	δ(1950)	S	K_{total}	U-J	J-F	F-N	N-K	r_1	z	Notes
9494	sa57	13:06:53.45	29:38:00.2	j	12.42 +0.00	-0.30 +0.09	0.63 +0.16	0.81 +0.16	2.19 +0.09	3.49	0.021	*J*2, *F*2, *N*1
7199	sa68	0:14:32.78	15:32:57.5	j	16.39 +0.10	-0.09 +0.04	0.63 +0.04	0.72 +0.05	1.96 +0.12	1.46	0.069	
7723	sa68	0:14:10.02	15:33:50.4	j	13.68 +0.08	0.02 +0.05	0.84 +0.05	0.75 +0.06	2.76 +0.11	2.59	0.078	
7880	sa68	0:14:12.18	15:34:05.1	j	14.19 +0.06	0.06 +0.04	0.88 +0.05	0.87 +0.04	2.37 +0.09	2.20	0.078	
12423	herc1	17:20:27.65	50:02:25.2	j	14.01 +0.08	0.17 +0.06	0.99 +0.07	0.95 +0.06	2.62 +0.09	1.75	0.085	
5016	herc1	17:19:58.93	49:48:34.5	j	14.29 +0.08	0.19 +0.07	0.85 +0.07	0.99 +0.06	2.49 +0.09	1.96	0.088	*J*1
9695	sa68	0:14:10.48	15:36:59.3	j	14.67 +0.06	0.12 +0.04	0.94 +0.04	0.84 +0.04	2.44 +0.08	2.33	0.093	
16159	sa68	0:15:03.07	15:48:06.8	j	16.15 +0.06	0.11 +0.05	0.95 +0.05	0.89 +0.05	2.22 +0.07	1.02	0.105	
3174	herc1	17:19:38.68	49:45:23.6	j	14.42 +0.06	-0.00 +0.04	0.75 +0.04	0.72 +0.04	2.17 +0.07	4.11	0.117	*K*
3414	herc1	17:20:12.54	49:45:44.8	j	13.30 +0.07	0.33 +0.06	1.20 +0.07	1.03 +0.06	2.56 +0.08	2.58	0.117	
8506	sa57	13:06:07.59	29:36:35.2	j	15.05 +0.03	0.06 +0.04	0.81 +0.04	0.72 +0.05	2.32 +0.08	1.95	0.123	
3162	herc1	17:19:20.66	49:45:23.9	j	14.74 +0.04	0.12 +0.06	1.06 +0.06	0.96 +0.05	2.47 +0.05	1.18	0.142	
13576	sa68	0:15:47.15	15:43:08.4	j	15.19 +0.06	0.07 +0.04	0.87 +0.04	0.86 +0.04	2.31 +0.08	1.56	0.153	
9285	sa68	0:14:04.28	15:36:18.8	j	14.86 +0.06	-0.02 +0.04	1.01 +0.05	0.96 +0.05	2.43 +0.08	1.63	0.159	
12006	sa68	0:15:33.52	15:40:32.3	j	15.43 +0.05	0.08 +0.05	1.08 +0.04	0.90 +0.04	2.63 +0.07	1.77	0.169	
6517	sa68	0:15:32.52	15:31:48.6	j	14.34 +0.05	0.00 +0.05	1.01 +0.06	0.87 +0.06	2.55 +0.09	1.87	0.172	
13222	herc1	17:20:43.27	50:04:02.6	j	14.55 +0.05	0.11 +0.07	1.20 +0.04	1.17 +0.06	2.91 +0.08	1.83	0.180	*z*1
12236	sa68	0:15:42.26	15:40:54.6	j	16.04 +0.16	-0.12 +0.04	0.91 +0.04	0.74 +0.06	2.47 +0.17	1.40	0.211	
7928	herc1	17:19:36.37	49:54:05.5	j	15.84 +0.30	-0.22 +0.04	0.87 +0.04	0.91 +0.04	2.89 +0.30	0.76	0.228	
11084	sa57	13:06:50.16	29:40:23.8	jz	13.90 +0.01	-0.32 +0.04	1.15 +0.04	0.81 +0.04	2.94 +0.04	2.90	0.243	
10356	sa68	0:14:10.11	15:37:56.7	z	16.03 +0.20	-0.27 +0.06	0.86 +0.05	0.82 +0.09	3.37 +0.33	1.11	0.302	
15534	sa68	0:14:31.39	15:46:53.0	z	16.77 +0.08	-0.41 +0.07	1.14 +0.05	0.80 +0.09	2.93 +0.15	0.71	0.303	
5154	sa68	0:14:42.01	15:29:43.5	jz	15.75 +0.14	-0.02 +0.05	0.87 +0.04	1.01 +0.05	2.77 +0.15	1.51	0.305	
10292	herc1	17:20:22.08	49:58:27.1	j	15.60 +0.04	-0.60 +0.08	0.42 +0.06	0.33 +0.07	2.00 +0.07	0.89	0.543	*U*2, *J*2, *F*2, *N*1, *K*, *AGN*

TABLE 6(c). Photometry, apertures, and redshifts for am and ak spectral-type galaxies.

NSER	Field	α(1950)	δ(1950)	S	K_{total}	U-J	J-F	F-N	N-K	r_1	z	Notes
10856	sa57	13:05:00.05	29:40:02.6	j	14.61 +0.07	0.05 +0.09	0.19 +0.09	0.30 +0.04	1.78 +0.07	2.83	0.018	*J2*
13616	hercl	17:19:47.78	50:05:02.2	j	13.91 +0.02	0.76 +0.07	1.34 +0.08	1.03 +0.08	2.48 +0.06	1.79	0.085	*F1*
11651	sa68	0:14:35.36	15:39:59.1	j	14.24 +0.05	0.80 +0.05	1.21 +0.07	1.07 +0.07	2.36 +0.09	1.51	0.094	
11859	hercl	17:20:04.60	50:01:21.3	j	14.04 +0.03	0.27 +0.05	1.13 +0.05	1.04 +0.05	2.57 +0.04	2.05	0.147	
15295	sa68	0:15:31.54	15:46:18.3	j	15.58 +0.03	0.26 +0.06	1.22 +0.04	1.03 +0.04	2.53 +0.06	1.00	0.153	
10153	sa68	0:13:55.50	15:37:39.4	j	14.72 +0.02	0.33 +0.04	1.18 +0.04	1.05 +0.04	2.78 +0.05	1.48	0.155	
18231	sa57	13:06:10.52	29:51:37.4	j	15.14 +0.04	0.13 +0.05	1.09 +0.04	0.74 +0.06	2.43 +0.07	1.68	0.160	
16664	sa68	0:14:31.36	15:49:18.7	j	14.87 +0.05	0.28 +0.05	1.14 +0.04	1.01 +0.04	2.73 +0.07	1.92	0.161	
16380	sa68	0:15:18.95	15:48:33.9	j	14.58 +0.06	0.23 +0.04	1.06 +0.04	0.91 +0.04	2.59 +0.07	2.34	0.165	
7001	sa68	0:15:00.22	15:32:34.8	j	14.59 +0.05	0.32 +0.04	1.28 +0.04	0.94 +0.04	2.72 +0.07	2.10	0.166	
11746	sa68	0:15:47.16	15:40:04.6	j	14.75 +0.04	0.54 +0.06	1.38 +0.05	1.01 +0.05	2.72 +0.06	1.65	0.176	
6356	sa68	0:15:31.09	15:31:33.5	j	14.61 +0.19	0.18 +0.04	1.21 +0.04	0.87 +0.04	2.82 +0.23	2.70	0.180	
17481	sa57	13:07:18.38	29:50:11.5	jz	14.33 +0.03	0.34 +0.13	1.25 +0.14	0.86 +0.15	2.67 +0.12	1.64	0.215	
10554	hercl	17:18:41.36	49:59:09.6	j	14.16 +0.03	0.08 +0.05	1.17 +0.05	0.89 +0.05	2.65 +0.05	2.07	0.227	
17778	hercl	17:19:47.92	50:14:46.0	j	14.95 +0.06	-0.00 +0.06	1.10 +0.04	0.98 +0.07	2.74 +0.09	1.74	0.229	
3176	hercl	17:19:33.37	49:45:24.4	j	14.52 +0.05	0.55 +0.12	1.44 +0.04	1.13 +0.06	2.89 +0.08	1.93	0.235	
12301	sa57	13:04:51.86	29:42:08.0	z	15.78 +0.03	-0.00 +0.07	1.12 +0.04	0.98 +0.08	2.37 +0.09	1.13	0.242	
11790	sa68	0:14:24.58	15:40:15.0	j	14.44 +0.02	0.13 +0.05	1.35 +0.06	1.05 +0.06	2.71 +0.06	1.36	0.250	
8317	hercl	17:18:37.08	49:54:53.9	j	15.80 +0.06	0.22 +0.05	1.48 +0.04	1.02 +0.04	2.31 +0.06	1.21	0.254	
10973	hercl	17:19:57.81	49:59:44.8	j	14.15 +0.04	0.23 +0.09	1.39 +0.04	1.24 +0.06	2.98 +0.06	2.37	0.287	
3756	hercl	17:18:05.19	49:46:37.9	j	14.26 +0.04	0.16 +0.04	1.45 +0.04	1.11 +0.04	2.93 +0.05	1.92	0.295	
14271	sa68	0:14:47.13	15:44:26.6	z	17.04 +0.05	-0.01 +0.13	1.14 +0.08	1.12 +0.11	2.52 +0.12	0.57	0.298	
7997	sa68	0:13:54.46	15:34:17.9	jz	14.85 +0.13	-0.12 +0.04	1.23 +0.04	1.06 +0.04	2.89 +0.14	1.78	0.303	
6024	sa68	0:15:13.64	15:31:03.4	jz	14.80 +0.43	-0.10 +0.04	1.18 +0.04	0.99 +0.04	2.98 +0.64	1.98	0.303	
5617	sa68	0:14:17.11	15:30:30.5	z	15.63 +0.05	0.58 +0.12	1.70 +0.04	1.08 +0.04	2.58 +0.08	1.02	0.307	
12670	sa68	0:14:48.37	15:41:40.7	z	17.74 +0.10	-0.10 +0.10	0.94 +0.07	0.94 +0.11	2.51 +0.15	0.51	0.310	
1279	sa68	0:15:00.22	15:22:14.7	j	14.75 +0.14	-0.04 +0.05	1.47 +0.04	1.05 +0.04	3.06 +0.18	1.43	0.350	

TABLE 6(d). Photometry, apertures, and redshifts for fm spectral-type galaxies.

NSER	Field	α(1950)	δ(1950)	S	K_{total}	U-J	J-F	F-N	N-K	r_1	z	Notes
1564	sa57	13:05:24.90	29:25:10.1	j	15.39 +0.08	0.26 +0.05	0.81 +0.04	0.77 +0.08	1.70 +0.11	3.47	0.023	
17315	sa68	0:15:05.86	15:50:53.9	j	15.83 +0.07	0.22 +0.05	0.89 +0.05	0.79 +0.05	1.90 +0.08	1.40	0.037	
8676	sa57	13:06:11.04	29:36:50.0	j	15.46 +0.09	0.25 +0.05	0.67 +0.04	0.45 +0.09	1.98 +0.12	3.65	0.056	
5009	hercl	17:20:31.58	49:48:28.1	j	14.02 +0.03	0.28 +0.05	0.93 +0.06	0.95 +0.05	2.26 +0.05	2.50	0.060	
6095	hercl	17:19:06.57	49:50:39.2	j	14.85 +0.07	0.29 +0.04	1.05 +0.04	0.89 +0.04	2.05 +0.07	2.67	0.073	
5389	sa68	0:14:37.73	15:30:07.1	j	13.56 +0.08	0.13 +0.04	0.83 +0.04	0.73 +0.04	2.86 +0.12	4.93	0.080	
3161	hercl	17:17:51.30	49:45:32.8	j	14.70 +0.06	0.13 +0.06	1.05 +0.06	0.80 +0.05	2.30 +0.06	1.74	0.082	
17050	hercl	17:18:58.66	50:13:09.7	j	14.08 +0.08	0.46 +0.06	1.20 +0.06	0.92 +0.07	2.44 +0.10	2.28	0.084	*J1*, *F1*
15439	hercl	17:18:20.67	50:09:18.5	j	13.73 +0.07	0.70 +0.06	1.40 +0.06	0.90 +0.07	2.50 +0.09	2.11	0.084	
6062	sa57	13:05:19.19	29:32:52.3	j	14.77 +0.04	0.23 +0.13	0.96 +0.14	0.88 +0.15	2.06 +0.12	2.35	0.084	
13618	hercl	17:18:53.93	50:05:09.6	j	15.99 +0.04	0.20 +0.04	0.94 +0.04	0.73 +0.04	2.06 +0.05	1.44	0.085	
13612	hercl	17:18:36.90	50:05:10.6	j	14.69 +0.04	0.37 +0.04	1.15 +0.04	1.00 +0.04	2.64 +0.05	1.44	0.087	
13213	sa68	0:14:45.95	15:42:38.2	j	15.17 +0.05	0.31 +0.04	1.10 +0.04	0.91 +0.04	2.52 +0.07	2.27	0.094	
11277	sa68	0:14:42.24	15:39:19.8	j	15.50 +0.06	0.18 +0.04	0.95 +0.04	0.84 +0.04	2.26 +0.08	2.21	0.094	
12487	sa68	0:15:02.48	15:41:21.3	j	12.82 +0.07	0.45 +0.05	1.26 +0.08	1.12 +0.13	2.66 +0.14	2.99	0.095	*J1*, *F1*, *N2*
16662	hercl	17:18:25.62	50:12:13.4	j	15.26 +0.05	0.26 +0.05	1.14 +0.04	0.88 +0.04	2.27 +0.05	1.66	0.100	
6357	hercl	17:20:00.66	49:51:01.4	j	13.85 +0.08	0.69 +0.06	1.37 +0.07	0.98 +0.08	2.50 +0.10	2.82	0.121	*F1*
14871	sa57	13:06:07.67	29:46:04.8	j	14.67 +0.02	0.30 +0.13	1.06 +0.14	0.80 +0.15	2.22 +0.12	1.90	0.122	
8069	hercl	17:19:24.63	49:54:22.1	j	14.76 +0.03	0.35 +0.06	1.19 +0.06	0.96 +0.06	2.24 +0.05	1.75	0.122	
7872	sa57	13:05:10.05	29:35:40.0	j	14.60 +0.06	0.61 +0.14	0.83 +0.16	0.58 +0.16	1.94 +0.13	2.13	0.128	*J2*, *F1*
12163	hercl	17:17:54.07	50:02:010.0	j	14.87 +0.04	0.33 +0.05	1.32 +0.05	0.83 +0.05	2.42 +0.05	1.40	0.138	
8541	hercl	17:18:47.19	49:55:17.7	j	15.11 +0.06	0.20 +0.05	1.05 +0.05	0.84 +0.05	2.31 +0.07	1.46	0.147	
10720	hercl	17:20:35.30	49:59:10.1	j	14.10 +0.05	0.67 +0.07	1.39 +0.05	1.07 +0.04	2.62 +0.06	1.97	0.155	
10463	hercl	17:17:18.24	49:59:06.2	j	13.51 +0.07	0.24 +0.08	1.28 +0.09	0.81 +0.07	2.85 +0.09	2.10	0.156	*J1*, *F1*
16944	sa57	13:07:00.33	29:49:23.0	j	14.52 +0.04	0.42 +0.13	1.17 +0.14	0.80 +0.15	2.34 +0.12	1.88	0.175	
17604	sa57	13:07:14.81	29:50:25.8	j	14.73 +0.03	0.23 +0.05	1.16 +0.04	0.82 +0.05	2.38 +0.07	2.14	0.176	
1906	hercl	17:20:010.00	49:43:06.5	j	14.44 +0.03	0.40 +0.08	1.34 +0.04	1.13 +0.06	2.56 +0.06	2.05	0.185	
1693	sa68	0:15:20.06	15:23:09.7	j	14.72 +0.03	0.56 +0.05	1.38 +0.04	0.98 +0.04	2.59 +0.05	1.73	0.210	
9243	sa57	13:06:00.49	29:37:41.1	z	14.77 +0.02	0.57 +0.10	1.49 +0.04	0.91 +0.06	2.66 +0.06	1.82	0.229	
12290	sa68	0:15:33.50	15:41:01.2	j	14.74 +0.46	0.49 +0.05	1.30 +0.05	0.94 +0.05	2.85 +0.64	2.02	0.235	
16599	sa57	13:06:50.46	29:48:49.5	z	15.18 +0.03	0.30 +0.07	1.36 +0.04	0.80 +0.07	2.51 +0.07	1.62	0.241	
12666	sa68	0:14:28.08	15:41:41.3	j	15.07 +0.14	0.76 +0.09	1.65 +0.05	1.08 +0.05	2.50 +0.17	1.63	0.251	
6217	sa68	0:14:26.36	15:31:24.3	z	15.53 +0.07	0.47 +0.12	1.63 +0.05	1.07 +0.05	2.84 +0.09	1.26	0.299	
6699	sa68	0:14:47.04	15:32:07.3	z	15.72 +0.04	0.78 +0.19	1.63 +0.05	1.09 +0.05	2.99 +0.09	0.74	0.302	
5841	sa68	0:14:49.94	15:30:47.7	z	15.10 +0.18	0.43 +0.09	1.59 +0.04	1.10 +0.04	2.97 +0.18	1.19	0.303	
17144	sa68	0:14:40.61	15:50:28.4	z	14.74 +0.08	0.98 +0.13	1.83 +0.04	1.20 +0.04	2.81 +0.08	1.46	0.311	

TABLE 6(e). Photometry, apertures, and redshifts for gm spectral-type galaxies.

NSER	Field	α(1950)	δ(1950)	S	K_{total}	U-J	J-F	F-N	N-K	r_1	z	Notes
16453	sa57	13:06:32.19	29:48:37.5	j	13.57 +0.03	0.64 +0.14	0.95 +0.15	0.54 +0.15	1.79 +0.12	2.84	0.023	$J1, F1$
4072	sa57	13:05:58.68	29:29:40.8	j	13.93 +0.05	0.43 +0.13	1.10 +0.14	0.72 +0.15	1.92 +0.12	3.83	0.023	$z1$
1289	sa57	13:06:13.63	29:24:25.0	j	14.26 +0.02	0.66 +0.14	1.17 +0.15	0.89 +0.15	2.15 +0.12	1.82	0.070	$J1, z1$
7975	hercl	17:17:06.45	49:54:24.6	j	14.90 +0.04	0.64 +0.06	1.17 +0.05	0.81 +0.05	2.23 +0.06	1.78	0.082	
17344	hercl	17:19:43.18	50:13:44.7	j	14.42 +0.03	0.57 +0.07	1.32 +0.05	1.05 +0.06	2.58 +0.05	1.60	0.084	
3869	sa57	13:07:17.79	29:29:20.8	j	13.13 +0.02	0.58 +0.13	1.26 +0.15	0.83 +0.16	2.23 +0.12	2.82	0.085	$J1, N1$
10081	sa68	0:14:10.69	15:37:34.4	j	13.09 +0.07	0.25 +0.04	1.01 +0.05	0.97 +0.05	2.97 +0.11	3.55	0.093	
3861	sa57	13:06:12.01	29:29:17.7	j	14.06 +0.02	0.67 +0.13	1.34 +0.15	0.73 +0.16	2.25 +0.12	2.39	0.116	$J1, F1, N1$
12508	sa57	13:05:57.12	29:42:29.0	s	15.16 +0.05	0.62 +0.14	1.33 +0.04	0.99 +0.09	3.00 +0.10	1.30	0.120	$z1$
16215	hercl	17:19:05.47	50:11:05.5	j	14.31 +0.13	0.89 +0.05	1.50 +0.06	0.98 +0.08	2.38 +0.14	1.37	0.121	$F1$
14852	sa57	13:06:07.38	29:46:03.6	s	15.73 +0.06	0.66 +0.12	1.24 +0.04	0.73 +0.10	2.30 +0.12	2.50	0.122	
11544	sa57	13:05:57.97	29:41:06.6	j	14.86 +0.04	0.79 +0.08	1.29 +0.04	0.80 +0.05	2.38 +0.06	1.83	0.122	
10962	sa57	13:06:06.37	29:40:13.8	j	14.99 +0.03	0.80 +0.08	1.30 +0.04	0.82 +0.05	2.46 +0.07	1.24	0.122	
16036	sa57	13:05:53.43	29:47:57.4	j	14.80 +0.03	0.78 +0.07	1.29 +0.05	0.88 +0.06	2.35 +0.08	1.69	0.123	
13044	sa57	13:05:57.61	29:43:15.8	j	14.16 +0.04	0.48 +0.05	1.26 +0.04	0.94 +0.04	2.62 +0.06	2.79	0.123	
12493	sa57	13:05:56.72	29:42:28.3	j	15.28 +0.05	0.81 +0.09	1.33 +0.04	0.85 +0.05	2.32 +0.07	0.91	0.123	
17300	sa57	13:05:46.01	29:50:01.0	j	14.52 +0.04	0.63 +0.13	1.34 +0.14	0.80 +0.15	2.48 +0.12	2.20	0.123	
6578	sa57	13:06:30.44	29:33:42.7	j	14.67 +0.07	0.52 +0.06	1.04 +0.04	0.88 +0.06	2.01 +0.09	3.34	0.123	
13343	sa57	13:05:35.85	29:43:39.3	j	14.17 +0.02	0.87 +0.06	1.26 +0.06	0.90 +0.10	2.27 +0.11	2.04	0.123	$J1, F1, N1$
12019	sa57	13:06:01.05	29:41:45.2	j	14.43 +0.04	0.65 +0.06	1.46 +0.05	0.83 +0.07	2.45 +0.08	1.92	0.123	
6463	sa57	13:07:11.67	29:33:29.8	j	13.32 +0.02	0.73 +0.13	1.53 +0.16	0.79 +0.18	2.44 +0.13	1.91	0.124	$J1, F1, N1$
14166	sa57	13:05:49.06	29:44:58.9	j	14.03 +0.03	0.66 +0.13	1.27 +0.15	0.86 +0.17	2.31 +0.14	2.75	0.124	$J1, F1, N1$
11014	sa57	13:06:04.84	29:40:17.9	j	12.65 +0.02	1.01 +0.07	1.36 +0.09	1.24 +0.12	2.31 +0.11	3.77	0.125	$J1, F2, N2$
4389	hercl	17:18:16.37	49:47:45.1	j	16.18 +0.09	0.63 +0.15	1.31 +0.04	0.90 +0.10	2.24 +0.14	1.00	0.130	$z2$
4309	hercl	17:18:16.33	49:47:37.4	j	15.64 +0.09	0.48 +0.12	1.14 +0.04	0.83 +0.11	2.51 +0.13	1.79	0.131	
14054	sa57	13:05:36.35	29:44:47.3	j	14.86 +0.03	0.86 +0.09	1.36 +0.04	0.86 +0.05	2.50 +0.05	1.43	0.136	
10005	sa57	13:05:02.17	29:38:43.5	j	14.45 +0.04	0.64 +0.05	1.26 +0.05	0.81 +0.05	2.35 +0.08	2.01	0.136	
14293	sa57	13:05:37.65	29:45:08.8	j	14.11 +0.03	0.73 +0.13	1.46 +0.14	0.87 +0.16	2.41 +0.13	1.79	0.137	$N1$
15041	sa57	13:05:40.76	29:46:20.2	j	15.05 +0.04	0.78 +0.08	1.40 +0.04	0.82 +0.05	2.38 +0.06	1.24	0.137	
3105	hercl	17:18:20.95	49:45:24.3	j	13.85 +0.02	0.66 +0.09	1.48 +0.05	1.07 +0.05	2.94 +0.05	2.21	0.142	
10849	hercl	17:20:30.12	49:59:26.1	j	14.60 +0.04	0.72 +0.05	1.37 +0.04	1.13 +0.04	2.41 +0.05	1.59	0.155	
3873	sa68	0:15:46.38	15:27:27.1	j	15.50 +0.05	0.86 +0.08	1.28 +0.04	0.89 +0.04	2.43 +0.07	1.68	0.157	
13756	sa57	13:06:36.77	29:44:18.5	j	14.35 +0.03	0.89 +0.08	1.36 +0.04	1.03 +0.04	2.49 +0.06	2.07	0.174	
10882	sa57	13:07:03.02	29:40:04.3	j	13.78 +0.03	0.79 +0.06	1.68 +0.05	0.89 +0.09	2.57 +0.10	2.33	0.187	$F1, N1$
7693	sa57	13:04:59.48	29:35:24.2	z	15.96 +0.04	1.17 +0.44	1.55 +0.05	1.39 +0.10	2.50 +0.11	1.04	0.223	
10468	sa57	13:05:47.77	29:39:27.8	z	14.90 +0.03	1.16 +0.22	1.59 +0.04	0.95 +0.07	2.81 +0.07	1.61	0.228	
10506	sa57	13:05:46.35	29:39:30.7	z	15.49 +0.02	1.11 +0.29	1.69 +0.04	1.04 +0.09	2.74 +0.09	0.96	0.229	
12482	sa57	13:05:57.49	29:42:27.5	s	15.92 +0.10	0.72 +0.36	1.73 +0.05	0.92 +0.16	2.96 +0.17	1.14	0.232	$z1$
9542	sa57	13:05:19.50	29:38:05.7	z	15.48 +0.03	1.11 +0.28	1.58 +0.04	1.06 +0.09	2.70 +0.09	1.23	0.233	
6840	hercl	17:19:41.90	49:52:00.9	j	14.65 +0.04	1.06 +0.18	1.55 +0.04	1.18 +0.06	2.65 +0.06	1.73	0.236	
10630	sa57	13:05:09.79	29:39:42.3	z	14.90 +0.03	0.84 +0.15	1.66 +0.04	0.96 +0.06	2.79 +0.07	1.42	0.237	
12260	sa57	13:05:28.72	29:42:06.1	z	14.60 +0.03	1.12 +0.18	1.71 +0.04	1.02 +0.05	2.87 +0.07	1.54	0.239	
12053	sa57	13:05:26.30	29:41:47.1	jz	13.47 +0.02	1.09 +0.10	1.34 +0.04	1.39 +0.04	2.69 +0.04	3.24	0.241	
11827	sa57	13:05:06.51	29:41:27.2	z	14.78 +0.03	1.10 +0.18	1.68 +0.04	1.01 +0.06	2.79 +0.07	1.62	0.242	
13900	sa57	13:05:35.55	29:44:30.2	z	14.79 +0.03	0.98 +0.14	1.65 +0.04	0.97 +0.05	2.76 +0.07	1.32	0.243	
5165	sa57	13:07:11.30	29:31:27.3	z	14.38 +0.03	0.88 +0.12	1.68 +0.04	1.13 +0.04	2.54 +0.06	2.02	0.247	
18052	hercl	17:19:59.38	50:15:26.3	j	14.41 +0.04	1.15 +0.30	1.76 +0.04	1.22 +0.07	2.91 +0.07	2.20	0.279	
7660	sa68	0:14:03.90	15:33:45.7	z	15.89 +0.06	0.57 +0.18	1.74 +0.06	1.29 +0.05	2.69 +0.09	0.82	0.301	
11061	sa68	0:15:13.32	15:38:58.4	z	16.96 +0.05	1.03 +0.44	1.76 +0.11	1.02 +0.10	2.65 +0.12	0.60	0.303	
13903	sa68	0:13:55.49	15:43:49.1	z	16.79 +0.13	1.13 +0.46	1.78 +0.10	1.13 +0.09	2.56 +0.15	0.71	0.308	
5110	hercl	17:20:25.84	49:48:40.4	j	14.03 +0.05	1.21 +0.27	1.71 +0.04	1.43 +0.06	2.93 +0.07	2.51	0.310	
3811	hercl	17:18:06.66	49:46:43.5	s	15.47 +0.09	1.07 +0.28	2.01 +0.08	1.24 +0.04	2.85 +0.08	1.82	0.363	$z1$

TABLE 6(f). Photometry, apertures, and redshifts for galaxies without spectral type.

NSER	Field	α(1950)	δ(1950)	S	K_{total}	U-J	J-F	F-N	N-K	r_1	z	Notes
6089	sa57	13:07:31.84	29:32:54.6	j	15.59 +0.08	...	0.71 +0.05	...	...	2.30	0.039	
191	sa57	13:06:01.11	29:21:14.3	jz	14.16 +0.03	...	1.36 +0.04	...	...	1.98	0.237	
16656	hercl	17:18:34.62	50:12:10.8	s	15.50 +0.08	...	2.08 +0.10	1.53 +0.14	3.04 +0.16	1.50	0.450	

Notes to TABLE 6

– Magnitudes and colors in this table are computed from the mean values of all flux measurements for each object and band. The photometric errors for each magnitude and color, computed from the positive root of the error function, are also given. These numbers begin with "+," and are immediately to the right of each magnitude or color. The positive root of the error function is defined as follows: For flux in band i, f_i, and flux error e_{f_i}, the quoted magnitude error, $e_{m_i,+}$, is:

$$e_{m_i,+} = 2.5\ log_{10}\ (\ 1 + e_{f_i}/f_i\ ).$$

For colors in bands i and j, $c_{i,j}$, the color error, $e_{c_{i,j},+}$, is:

$$e_{c_{i,j},+} = 2.5\ log_{10}\ (\ 1 + \sqrt{(e_{f_i}/f_i)^2 + (e_{f_j}/f_j)^2}\ ).$$

The flux errors for the individual bands can be derived explicitly from these formulae. Note that magnitude errrors for the photographic photometry have a conservative minimum value of 0.03 magnitudes. Colors use magnitudes measured within matching apertures and are calibrated as discussed in Sections 3.2.3 and 3.2.4.

– The K band total magnitude, K_{total}, defined in Sections 3.2.2-3.2.4, represents the flux measured within an aperture of radius $2r_1$, where r_1 is determined in the K band.

*U*1: U photographic photometry saturation correction is between 0.1 – 0.2 magnitudes.
*U*2: U photographic photometry saturation correction is > 0.2 magnitudes.
*J*1: J photographic photometry saturation correction is between 0.1 – 0.2 magnitudes.
*J*2: J photographic photometry saturation correction is > 0.2 magnitudes.
*F*1: F photographic photometry saturation correction is between 0.1 – 0.2 magnitudes.
*F*2: F photographic photometry saturation correction is > 0.2 magnitudes.
*N*1: N photographic photometry saturation correction is between 0.1 – 0.2 magnitudes.
*N*2: N photographic photometry saturation correction is > 0.2 magnitudes.

K: K band photometry may be more uncertain than indicated due to observing conditions.

*z*1: The spectroscopic redshift is uncertain, but agrees with color-estimated redshift to within accuracy of esimate (± 0.05 in redshift).
*z*2: Redshift is estimated from colors only, with uncertaintly of ± 0.05 in redshift.

AGN: Galaxy has broad-lined emission spectrum

Since the uncertainty in $E(B-V)$ is considerably larger than 0.02 mag, we apply *no* reddening correction to our data.

4. THE PHOTOMETRIC DATA

4.1 Data Tables

The final optical and near-infrared photometry of the 176 galaxies in our *K* band imaging survey is presented in Table 6. This sample is defined in Tables 2(a) and 2(b), but includes 5 additional, serendipitous objects as described in Sec. 2. The photometry has been measured, calibrated, and otherwise corrected as described in Sec. 3. *These data are used in our subsequent analysis in paper II.* In addition to magnitudes and colors, we include the radius r_1, defined in Sec. *3.2.2*. The purpose of including this size information is to allow future studies to compare new photometry of these objects reliably to our data. Such a comparison must be done within comparable apertures, and calibrated in such a way as to account for changes in image resolution (see Sec. *3.2.4*). However, we warn that the tabulated r_1 should *not* be considered reliable measures of intrinsic size, since the effects of seeing are frequently significant and *not* correctable without detailed profile and seeing information (neither of which has been provided). Finally, we have included the spectroscopic redshift of each galaxy.

For the purpose of facilitating paper II, galaxies have been tabulated in five groups [Tables 6(a)–6(e)] according to the spectral types derived in paper II: bg and bk, bm, ak and am, fm, gm. A sixth table, 6(f), contains three galaxies without *U*, and/or *N* photometry, or spectral types.

In each table, column (1) contains the object serial number from the parent catalogues, column (2) contains the field name, and columns (3) and (4) contain the Right Ascension and Declination (1950). Column (5) contains the sample descriptor, S: j for the magnitude limited sample of Table 2(a); z for the color–redshift sample of Table 2(b); and s for serendipitous.

Columns (6)–(15) are in pairs representing magnitudes or colors and their estimated uncertainty. Only the positive root $(+\sigma)$ of the magnitude error function is given, as defined in the Notes to Table 6. Formulas are provided therein for the derivation of other error estimates. There is a lower limit imposed of 0.03 mag for the uncertainty in each optical band, prior to any increase due to uncertainty in the saturation correction. No lower limit has been stipulated for the uncertainty in the *K* band magnitude. Columns (6) and (7) contain the *K* band total magnitude, determined within the near-infrared $2r_1$ aperture. Matching aperture magnitudes are used in columns (8) through (15) to produce $U-J$, $J-F$, $F-N$, and $N-K$ colors and estimated uncertainties, respectively.

Column (16) contains the *K* band r_1 radius in arcseconds.

Column (17) contains the spectroscopic redshift (except where indicated).

Column (18) contains codes denoting potentially unreliable photometry or redshifts, as described in the Notes to Table 6.

4.2 Images

Figures 16(a)–16(f) (Plates 21–26) contain the first optical and near-infrared atlas of a statistically representative sample of field galaxies. Traditionally, catalogued galaxies are classified according to some morphological type (e.g., the Hubble sequence). However, from inspection of the images (in either the optical or near-infrared), it was clear to us that morphological classification would be particularly prone to distance-dependent biases due to the change in apparent size and hence resolution of the sample as a function of redshift. As we will discuss again in paper II, traditional morphological classification is highly subjective and not clearly useful for cosmological studies relative to other classification schemes, e.g., color types, or the Yerkes spectral type (Morgan & Mayall 1957). Galaxies have been separated into five groups according to our spectral types (paper II). For each type, galaxies are displayed as a function of redshift. Figures 16(a)–16(f) reveal the change in apparent size and resolution with redshift while at the same time display the variety of apparent morphology for galaxies of comparable colors.

5. DISCUSSION

Here we examine the final galaxy photometry to assess the field-to-field uniformity as well as the absolute calibration of the colors. The latter assessment is made by comparing color–color and color–redshift distributions to models, e.g., Bruzual & Charlot (1993). In exploring the broadband spectral properties of galaxies, the color–color as well as color–redshift distributions offer complementary information. Color–redshift distributions allow one to unambiguously disentangle the effects of redshift from the intrinsic range of galaxy colors. However, it is often only in color–color diagrams that peculiar objects will stand out (e.g., QSOs, or uncorrelated magnitude errors). With this in mind, in Fig. 17 we have plotted a complete set of color–color distributions for all colors formed from adjacent bands. Only galaxies brighter than $J=19.65$ are plotted, a selection which provides a fair field-to-field comparison and limits the observed redshift range to $0<z<0.25$. The latter in turn limits the range of apparent colors. To complement these figures, the color–redshift distributions for our entire sample for the same set of colors are shown in Fig. 18, extending to $z=0.55$.

In both Figs. 17 and 18, we compare the galaxy distributions to nonevolving galaxy models (Bruzual & Charlot 1993) for extreme star-formation rates and an age of 16 Gyr. We also include simulated colors as a function of redshift based on observed spectral energy distributions of local elliptical galaxies (two averages), as well as an extreme star-forming galaxy (N4449). This set (referred to as the "models") provides extrema at both the red and blue end of the expected galaxy color distributions: although there will be some galaxies bluer or redder than the models, such objects should be relatively few in number.

For the color–color diagrams, we expect galaxies to lie not only within the blue and red model extrema, but also within the boundaries imposed by the upper and lower observed redshift limits and the continuum of galaxy colors at each of these redshifts. To simulate these redshift boundaries, we have used model galaxies of intermediate star-formation rate (also 16 Gyr in age). The result is an effective area within which we expect galaxies to lie.

First consider the relative and absolute calibration of the photometry for the galaxies taken as a statistical sample. Inspection of the color–color and color–redshift diagrams reveals that across fields the locus of galaxies overlap and span the same range. In the color–color plots, the distribution perpendicular to the galaxy locus is dictated by the redshift distribution, whereas the distribution along the galaxy locus is determined by the galaxy mix (i.e., spectral type) at each redshift. For example, there are a relatively larger number of blue galaxies in SA68 and SA57 than in Herc 1, *but the range of colors is comparable for all fields*. This can be seen even more clearly in Fig. 18. At redshifts between 0.2–0.3 in the color–redshift diagrams, there are of course differences between fields because of the bias of the color–redshift selected samples. However, at lower redshifts, the range of colors in all bands between fields is comparable. The absence of color offsets between fields indicates good relative calibration in all colors. Also note that galaxies lie squarely centered in color between the model limits. This testifies to the absolute calibration of the colors.

Next consider individual galaxies that are outliers in Figs. 17 and 18. Such objects may have unreliable photometry *or* may simply represent the tails of galaxy color distributions. We try to assess both possibilities. In these figures, we have marked objects which have large saturation corrections (>0.2 mag in at least one band), as well as objects with uncertain redshifts. In addition, the photometric errors of all outlying objects have been marked.

We find that isolated, outlying galaxies in the color–color diagrams are either within 1–2 sigma of the expected colors or are heavily saturated, with few, but notable, exceptions. These exceptions are sa57.11084 and sa57.12053. The former is a highly disturbed, interacting, and superluminous galaxy at $z=0.24$, with atypical colors in Figs. 17(a) and 17(c). The morphology of this object is exceptionally wavelength dependent, as demonstrated by Majewski (1988), and seen here in Fig. 16. The latter is the cD galaxy in the Zwicky cluster II Zw 1305.4+2941, (Koo *et al.* 1986b), also at $z=0.24$, with atypical colors in Figs. 17(a)–17(c), as well as in Fig. 18 for $F-N$ vs redshift. These objects are exceptional in almost all of their characteristics (size, shape, luminosity), and therefore it is not clear that their colors are in error.

Two other objects, sa68.7723 and sa68.5389, have marginally extreme colors in Fig. 17(c) ($F-N$ vs $N-K$). Their total magnitudes are bright but are not saturated on any of the plates. Their spectra reveal strong Hα emission, however we cannot tell whether the emission is broad due to the resolution of our spectra. An inspection of their image structure shows they do have bright, compact stellar nuclei embedded in otherwise disk-like systems. Given the N-K colors found for the QSO candidate displayed in Fig. 11, it is plausible that these are Seyfert Galaxies. However, these objects were observed at Lick using PNIC (see Sec. *3.1.3*), and it is also conceivable that their K photometric errors are larger than

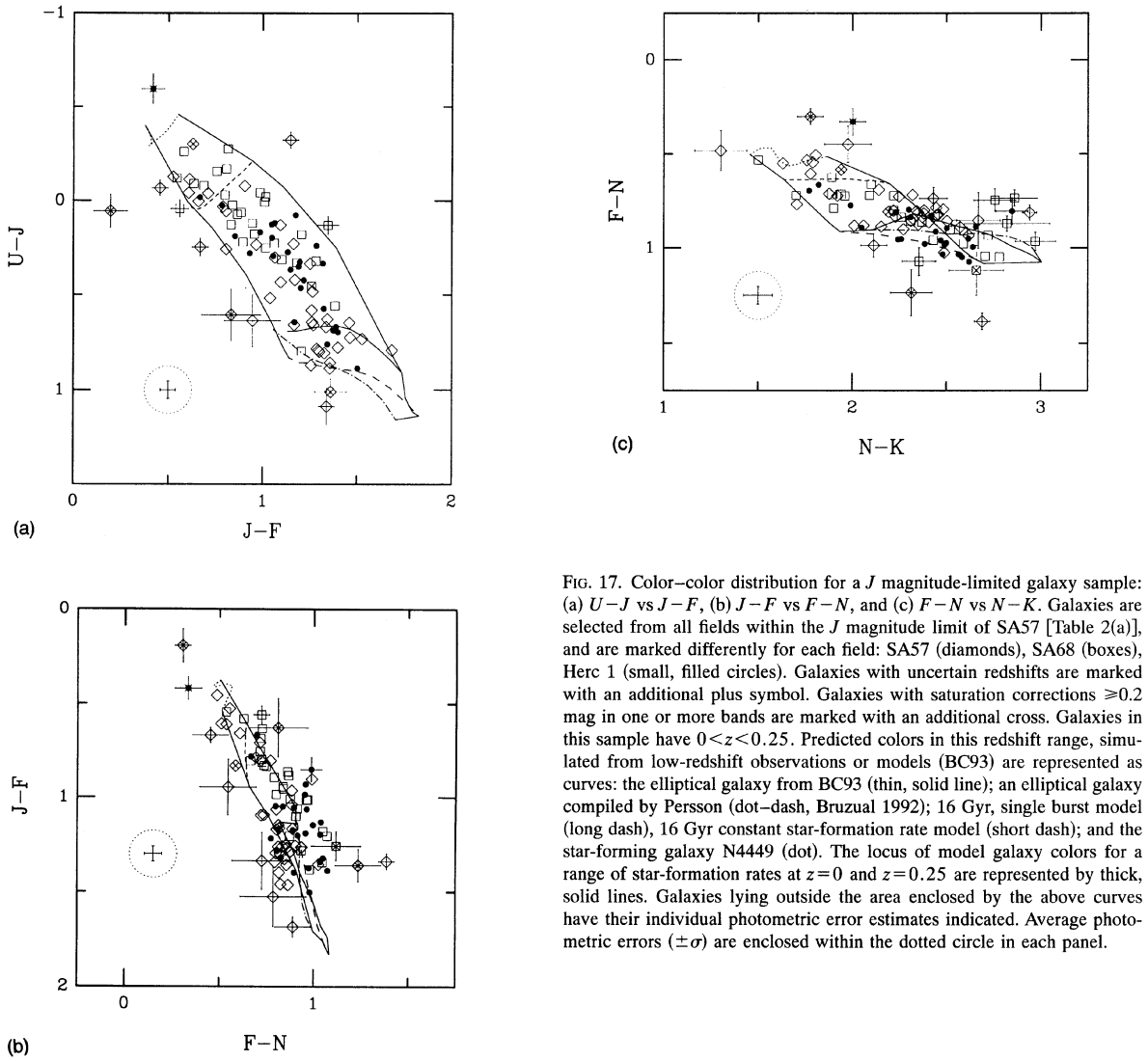

FIG. 17. Color–color distribution for a J magnitude-limited galaxy sample: (a) $U-J$ vs $J-F$, (b) $J-F$ vs $F-N$, and (c) $F-N$ vs $N-K$. Galaxies are selected from all fields within the J magnitude limit of SA57 [Table 2(a)], and are marked differently for each field: SA57 (diamonds), SA68 (boxes), Herc 1 (small, filled circles). Galaxies with uncertain redshifts are marked with an additional plus symbol. Galaxies with saturation corrections ≥ 0.2 mag in one or more bands are marked with an additional cross. Galaxies in this sample have $0<z<0.25$. Predicted colors in this redshift range, simulated from low-redshift observations or models (BC93) are represented as curves: the elliptical galaxy from BC93 (thin, solid line); an elliptical galaxy compiled by Persson (dot–dash, Bruzual 1992); 16 Gyr, single burst model (long dash), 16 Gyr constant star-formation rate model (short dash); and the star-forming galaxy N4449 (dot). The locus of model galaxy colors for a range of star-formation rates at $z=0$ and $z=0.25$ are represented by thick, solid lines. Galaxies lying outside the area enclosed by the above curves have their individual photometric error estimates indicated. Average photometric errors ($\pm\sigma$) are enclosed within the dotted circle in each panel.

indicated (see Sec. *3.3.3*). An object with similar colors, but somewhat less discrepant, herc1.10463, was also observed with PNIC. On the other hand, sa57.11084 has comparable and outlying colors and was observed with the IRIM. Therefore our interpretation of the cause for these outlying colors (astrophysical or due to observational error) is inconclusive.

Note that the color distribution in $J-F$ vs $F-N$ [Fig. 17(b)] is broader than anticipated from the models. This effect is largely in $F-N$, as seen in Fig. 18. Because there are so many galaxies at all redshifts, apparent magnitudes, and fields that are redder than the reddest model, the observed colors are very likely to be real. Because the models well define the blue limit of the galaxy distribution in $F-N$ in Fig. 18, as well as track the colors with redshift (recall that the reddest galaxies in $F-N$ have been preferentially observed between $0.2<z<0.3$), it is unlikely that this discrepancy is due to a zero-point mismatch between models and data. Indeed, all of our previous results from Sec. 3 imply just the opposite. Unless we have grossly underestimated our photometric errors for the N band, it appears instead that the models have an insufficient dynamic range to the red for colors spanning the wavelength range of 0.55 to 0.9 μ. Earlier models also appear to not reach sufficiently red $F-N$ colors compared to our or similar photographic data (Bruzual 1986; Guiderdoni & Rocca-Volmerange 1988).

Finally, we consider objects with exceptional colors found only in Fig. 18. $U-J$ and $J-F$ colors are all consistent with the models, but several objects have exceptionally red $F-N$ and $N-K$ colors. For $F-N$ these objects are herc1.5110 and sa57.7693, as well as sa57.12053 (mentioned above). These objects are significantly redder than even the large number of objects that are somewhat redder than the reddest model. For $N-K$, sa68.5389, sa68.10081, sa57.12508, and herc1.3105 are exceptionally red. Only two of the latter set were observed with PNIC (sa68.5389 and sa68.10081). Although there may be photometric problems with some of these data, the heterogeneous nature of these outlying objects in terms of field and apparent magnitude, as well as the source of near-infrared photometry (PNIC vs IRIM), precludes any simple explanation. These objects do not suffer from any

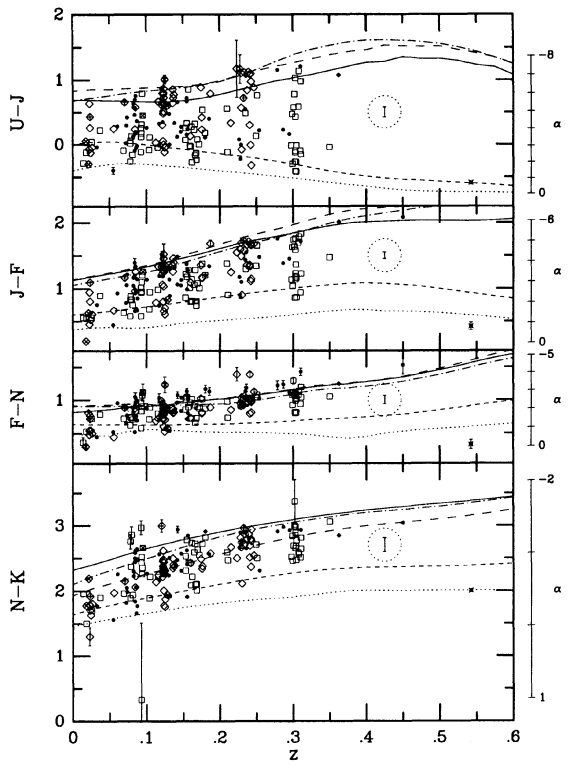

FIG. 18. Color–redshift diagrams for $U-J$, $J-F$, $F-N$, and $N-K$ for all galaxies in our sample. Symbols are as in Fig. 17. Predicted colors from low-redshift observations or models (BC93) are represented as curves as described in Fig. 17. Objects which lie to the red or blue of these predicted colors have their photometric errors marked. Average photometric errors ($\pm\sigma$) for the entire sample are enclosed within the dotted circle in each panel. To the right of each panel, a scale indicates color as a function of the power-law index α ($f_\nu \propto \nu^\alpha$).

significant photographic saturation. In light of these results, such objects may just as well represent a true tail in the distribution of galaxy colors.

In closing, note that we can also interpret the results presented in Figs. 17 and 18 as a vindication of the models of Bruzual & Charlot (1993). We have shown for the first time that such models well represent the range and trends with redshift (to $z=0.3$) of galaxy colors spanning 0.37 to 2.2 μ.

6. SUMMARY

We have presented a photometric analysis of optical and near-infrared images of a statistically complete galaxy sample. This study has been based on existing *UJFN* photographic photometry and a new K band imaging survey of over 170 optically selected field galaxies with spectroscopic redshifts.

We have established the uniformity of the photometric apertures and calibration in all bands, and explored possible systematic aperture effects due to different galaxy morphology. A robust algorithm for measuring galaxy total magnitudes based on the first moment of the light distribution has been defined, tested, and compared to previous algorithms. We have shown that (1) systematics due to changes in seeing largely can be eliminated from galaxy photometry through appropriate calibration procedures; and (2) aperture effects on the integrated colors due to color gradients are negligible for our photometry.

Photographic saturation substantially effects 12% of our galaxy sample in one or more bands. However, we have determined a saturation correction for these objects using the measured saturation properties of stars and the measured plate density distributions for stars and galaxies. Only 3% of the galaxies in this survey have corrections larger than 0.2 mag; only for these 3% are the derived saturation corrections likely to be inaccurate. The vast majority of objects thus have reliable photometry.

The photometric zero-point of our optical-infrared colors for serendipitously observed stars agrees with independent predictions of the spectral library compiled by Persson (1987) and by Bruzual (BC93). This provides a direct check on the absolute calibration of our photometric data. The color–color and color–redshift distributions of galaxies lie squarely between nonevolving model and empirical galaxy colors. This further attests to the absolute calibration of our photometry. The galaxy color distributions are uniform between different fields, which demonstrates the accurate relative calibration of the photometry.

Finally, our photometric data as well as spectroscopic redshifts have been tabulated, replete with information indicating the accuracy of each measurement. This reliable data set will enable us to determine the range of and better understand the intrinsic dispersion in galaxy colors to cosmologically interesting redshifts.

Research was primarily supported by a NASA graduate fellowship to M.A.B. (NGT 50677), and NSF Grants Nos. AST-87-05517 and AST-88-14251. M.A.B. and S.R.M. acknowledge support from NASA through Grants Nos. HF-1028.01-92A and HF-1036.01-92A, respectively, from the Space Telescope Science Institute, which is operated by the Association of Universities for Research in Astronomy, Incorporated, under Contract No. NAS5-26555. M.H. was supported by the Astrophysical Research Consortium and by the National Science Foundation under a cooperative agreement with the Center for Astrophysical Research in Antarctica (CARA), Grant No. NSF DPP 89-20223. D.C.K. acknowledges support from NSF Grant No. AST-88-58203. We are indebted to several people who made their data available to us in advance of publication, in particular G. Bruzual for his spectral library, and D. Trevese for his catalogues. R. Bell provided his models atmospheres, and R. Probst provided the filter transmission curves for the IRIM. L. Infante and C. Pritchet also provided their photometric catalogue prior to publication. We thank R. Probst and D. Joyce at KPNO for their support and help using the IRIM, R. Kraft at Lick Observatory for supporting the use of PNIC on the Shane 3 m telescope, and D. Chamberlin and other telescope assistants at KPNO and Lick for putting up with over 500 telescope dithers per night. We also thank S. Jansen and S. Polishinski at MADRAF for their support of the PDS; M. Wasow for her hospitality; R. Greene and E. Carter at KPNO for their support of the PDS and helpful discussion; and K. Cudworth, D.

Trevese, and E. Kibblewhite for helpful discussions in this regard. D. York and D. Lamb who graciously provided the use of their computers during the early part of this project. We also acknowledge P. McMillan (Media Services, UCSC) for his assistance in producing high-quality prints for our figure-plates.

REFERENCES

Aaronson, M. 1977, Ph.D. thesis, Harvard University
Bershady, M. A. 1994, AJ (submitted) (Paper II)
Bershady, M. A., Hereld, M., Kron, R. G., & Koo, D. C. 1990, in Astrophysics with Infrared Arrays, edited by R. Elston (ASP, Provo), 14, 9
Bershady, M. A., Trevese, D., & Kron, R. G. 1991, in Variability of Active Galactic Nuclei, edited by H. Miller and P. Wiita (Cambridge University), 67
Boulanger, F., & Perault, M. 1988, ApJ, 330, 964
Brooks, K. 1981, Ph.D. thesis, University of California, Berkeley
Bruzual, A. G. 1981, Ph.D. thesis, University of California, Berkeley
Bruzual, A. G. 1986, in Spectral Evolution of Galaxies, edited by C. Chiosi and A. Renzini (Kluwer, Dordrecht) p. 263
Bruzual, A. G. 1992, private communication
Bruzual, A. G., & Charlot, S. 1993, ApJ, 405, 538
Bunclark, P. S., & Irwin, M. J. 1983, Proc. Symposium Statistical Methods in Astronomy (Strousbourg), ESA SP-201
Burstein, D., & Heiles, C. 1982, AJ, 87, 1165
Chokshi, A., & Wright, E. L. 1987, ApJ, 319, 44
Cowie, L. L., Lilly, S. J., Gardner, J. P., Lilly, S. J., & McLean, I. 1988, ApJ, 332, L29
Cowie, L. L., Songalia, A., & Hu, E. M. 1992, Nature, 354, 460
de Vaucouleurs, G. 1961, ApJS, 5, 233
de Vaucouleurs, G., de Vaucouleurs, A., & Corwin, H. G. 1976, Second Reference Catalogue of Bright Galaxies (University of Texas, Austin) (RC2)
Dressler, A., & Gunn, J. E. 1992, ApJS, 75, 1
Elias, J. H., Frogel, J. A., Matthews, K., & Neugebauer, G. 1982, AJ, 87, 1029
Ellis, R. S. 1980, PTRSL, 296, 355
Ellis, R. S., & Allen, D. A. 1983, MNRAS, 203, 685
Elston, R., Rieke, M. J., & Rieke, G. H. 1988, ApJ, 331, L77
Elston, R., Rieke, M. J., & Rieke, G. H. 1989, ApJ, 341, 80
Frogel, J. A. 1985, ApJ, 298, 528
Frogel, J. A., Persson, S. E., Aaronson, M., & Matthews, K. 1978, ApJ, 220, 75
Grasdalen, G. L. 1975, ApJ, 195, 605
Griersmith, D., Hyland, A. R., & Jones, T. J. 1982, AJ, 87, 1106
Guiderdoni, B., & Rocca-Volmerange, B. 1988, A&AS, 74, 185
Gunn, J. E., & Oke, J. B. 1975, ApJ, 195, 255
Gunn, J. E., & Stryker, L. L. 1983, ApJS, 52, 121
Hall, P., & Mackay, C. D. 1984, MNRAS, 210, 979
Hereld, M., Harper, D. A., Pernic, R. J., & Rauscher, B. J. 1990, in Instrumentation in Astronomy VII, edited by D. Crawford, Proc. SPIE 1235, 84
Hoessel, J. G. 1980, ApJ, 241, 493
Huchra, J. P. 1977, ApJS, 45, 171
Infante, L. 1987, A&A, 183, 177
Infante, L., & Pritchet, C. J. 1992, ApJS, 83, 237
Johnson, H. L. 1965, ApJ, 141, 923
Johnson, H. L. 1966, ARA&A, 4, 193
Koo, D. C. 1985, AJ, 90, 418
Koo, D. C. 1986, ApJ, 311, 651
Koo, D. C., Bershady, M. A., Wirth, G. D., Stanford, S. A., & Majewski, S. R. 1994, ApJ, 427, L9
Koo, D. C., Ellman, N., Kron, R. G., Munn, J. A., Szalay, A. S., Broadhurst, T. J., & Ellis, R. S. 1992, in Proceedings of 6th Marcel Grossman Meeting on General Relativity, edited by H. Sato and T. Nakamura (World Scientific, Singapore), p. 17
Koo, D. C., & Kron, R. G. 1982, A&A, 105, 107
Koo, D. C., & Kron, R. G. 1988a, ApJ, 325, 92
Koo, D. C., & Kron, R. G. 1988b, in Towards Understanding Galaxies at Large Redshift, edited by R. G. Kron and A. Renzini (Kluwer, Dordrecht), p. 209
Koo, D. C., Kron, R. G., & Cudworth, K. M. 1986a, PASP, 98, 285
Koo, D. C., Kron, R. G., Nanni, D., Trevese, D., & Vignato, A. 1986b, AJ, 91, 478
Kormendy, J. 1973, AJ, 78, 255
Kron, R. G. 1980, ApJS, 43, 305
Kron, R. G., Bershady, M. A., Munn, J. A., Smetanka, J. J., Majewski, S. R., & Koo, D. C. 1991, in The Space Distribution of Quasars, ASP Conference Series, edited by D. Crampton (ASP, San Francisco), pp. 21, 32
Kron, R. G., & Chiu, L-T. G. 1981, PASP, 93, 397
Kurucz, R. L. 1979, ApJS, 40, 1
Lilly, S. J., Cowie, L. L., & Gardner, J. P. 1991, ApJ, 369, 79
Majewski, S. R. 1988, in Towards Understanding Galaxies at High Redshift, edited by R. G. Kron and A. Renzini (Kluwer, Dordrecht), p. 203
Majewski, S. R. 1992, ApJS, 78, 87
Majewski, S. R., Munn, J. A., Kron, R. G., Bershady, M. A., Smetanka, J. J., & Koo, D. C. 1991, in The Space Distribution of Quasars, ASP Conference Series, edited by D. Crampton (ASP, San Francisco), pp. 21, 55
Manduca, A., & Bell, R. A. 1979, PASP, 91, 848
Mobasher, B., Ellis, R. S., & Sharples, R. M. 1986, MNRAS, 223, 11
Morgan, W. W., & Mayall, N. U. 1957, PASP, 69, 291
Munn, J. A., Koo, D. C., Kron, R. G., Bershady, M. A., Smetanka, J. J., & Majewski, S. R. 1994, in preparation
Nanni, D., Pittella, G., Trevese, D., & Vignato, A. 1980, in Two Dimensional Photometry, edited by P. Crane and K. Kjar (ESO Workshop Proceedings), p. 329
Persson, S. E. 1987, unpublished
Probst, R. 1992, personal communication
Renzini, A., & Buzzoni, A. 1986, in Spectral Evolution of Galaxies, edited by C. Chiosi and A. Renzini (Reidel, Dordrecht), p. 195
Sandage, A. 1972, ApJ, 173, 485
Smetanka, J. J. 1993, MNRAS (submitted)
Stetson, P. B. 1979, AJ, 84, 1056
Storm, J., Carney, B. W., & Latham, D. W. 1992, PASP, 104, 159
Strecker, D. W., Erickson, E. F., & Witterborn, F. C. 1979, ApJS, 41, 501
Strecker, D. W., Erickson, E. F., & Witterborn, F. C. 1989, unpublished
Trevese, D., Pittella, G., Koo, D. C., Kron, R. G., & Bershady, M. A. 1989, AJ, 98, 108
Tully, R. B., Mould, J. R., & Aaronson, M. 1982, ApJ, 257, 527
Tyson, J. A. 1984, PASP, 96, 566
Tyson, J. A. 1988, AJ, 96, 1
Valdes, F. 1982, Proc. SPIE, 331, 465
Vandenberg, D. A., & Bell, R. A. 1985, ApJS, 58, 561
Visvanathan, N. 1981, A&A, 100, L20
Windhorst, R. A., Kron, R. G., & Koo, D. C. 1984, A&A, 58, 39
Wyse, R. 1982, MNRAS, 199, 1P
Wyse, R. 1985, ApJ, 299, 593

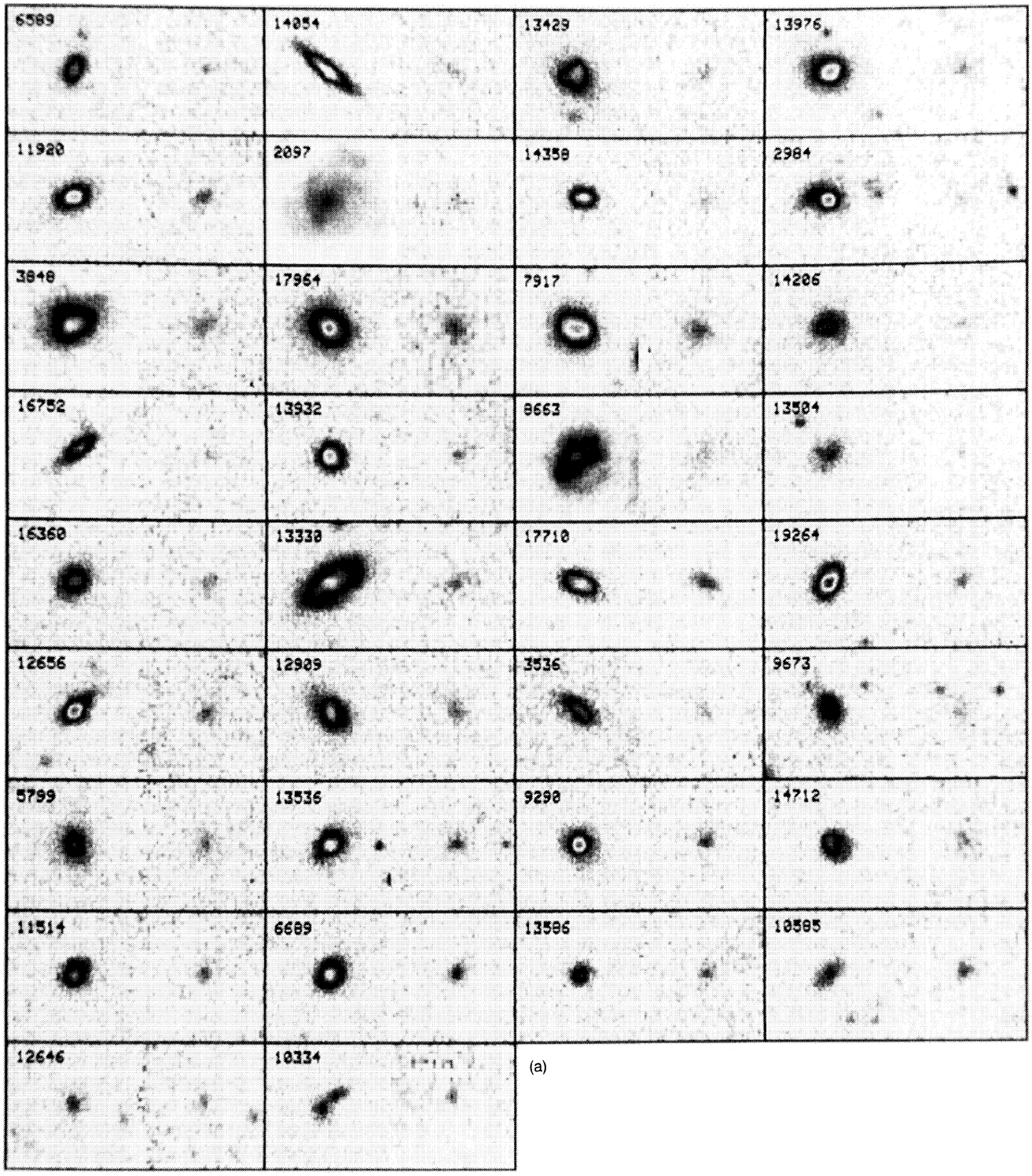

FIG. 16. *A J(B)* and *K* band image montage of our entire galaxy sample is presented. Objects in each panel are sorted by redshift to match Table 6. Objects in panels (a)–(f) are distinguished by spectral types, respectively, bk and bg, bm, am and ak, fm, and gm [panels (e) and (f)]. Images are 20 arcsec on a side, and the intensities are displayed logarithmically using a double saw-tooth look-up table. Panel (a) is above (bk and bg spectral-type galaxies).

Bershady *et al.* (see page 892)

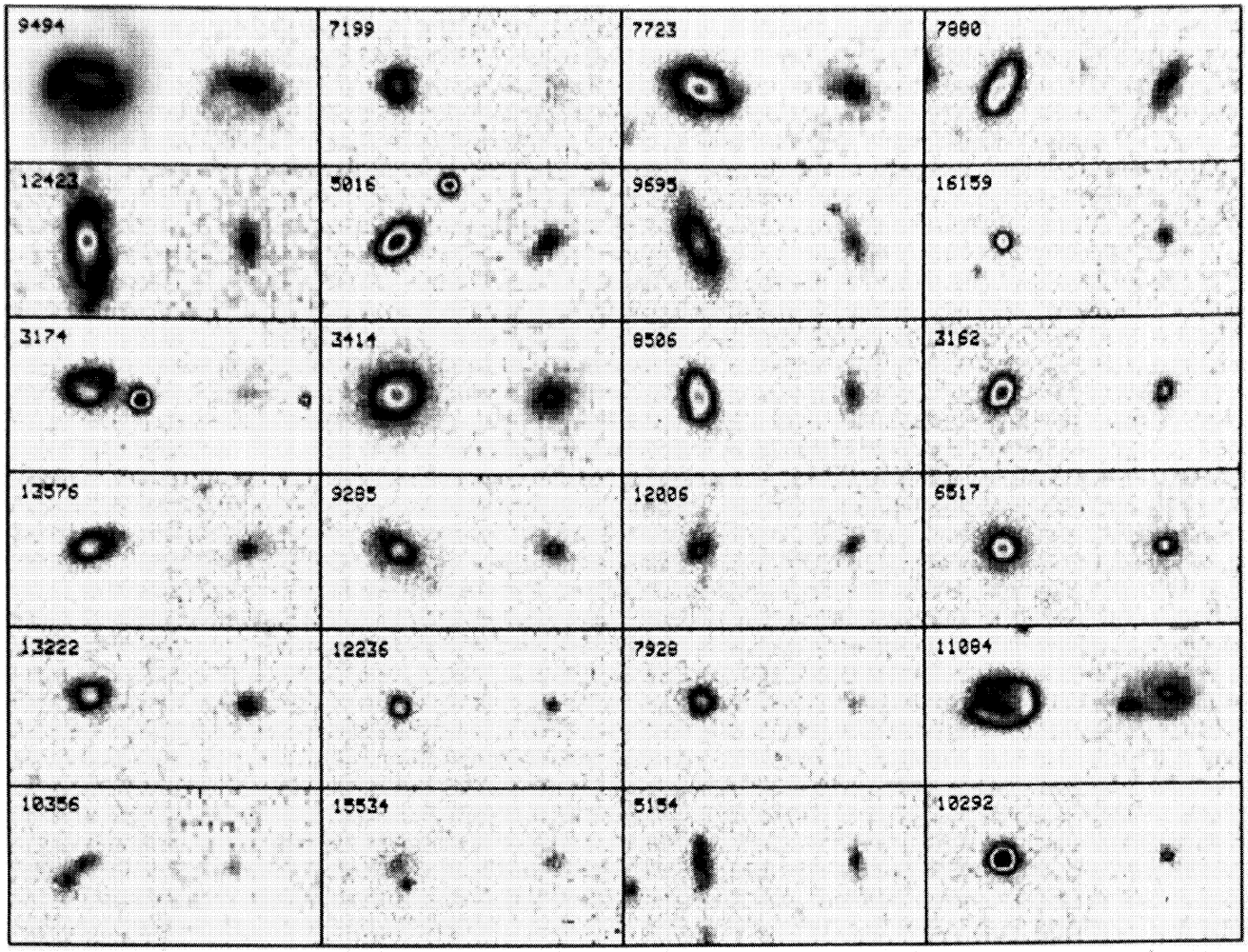

(b)

FIG. 16. (b) bm spectral-type galaxies.

Bershady *et al.* (see page 892)

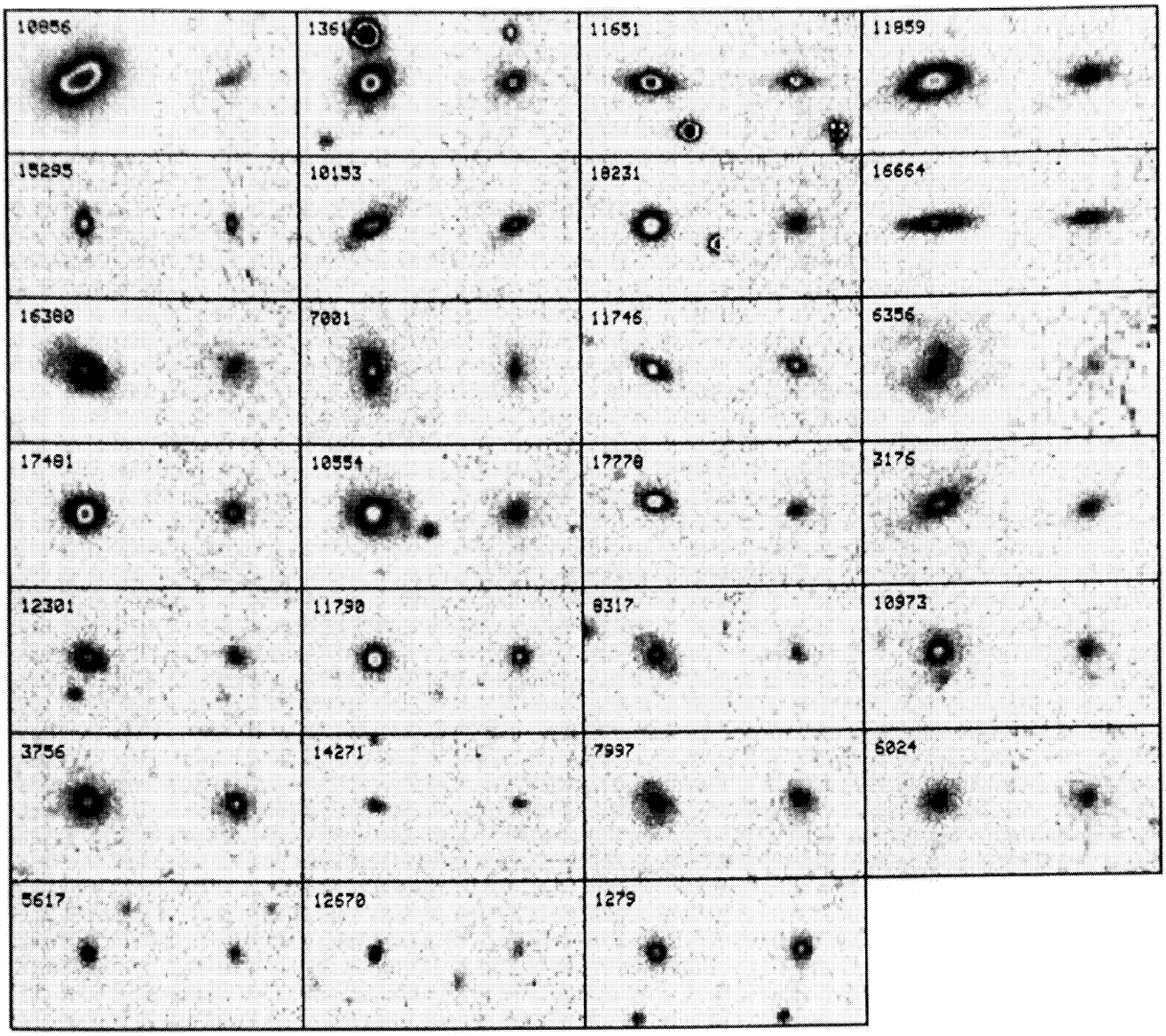

(c)

FIG. 16. (c) am and ak spectral-type galaxies.

Bershady *et al.* (see page 892)

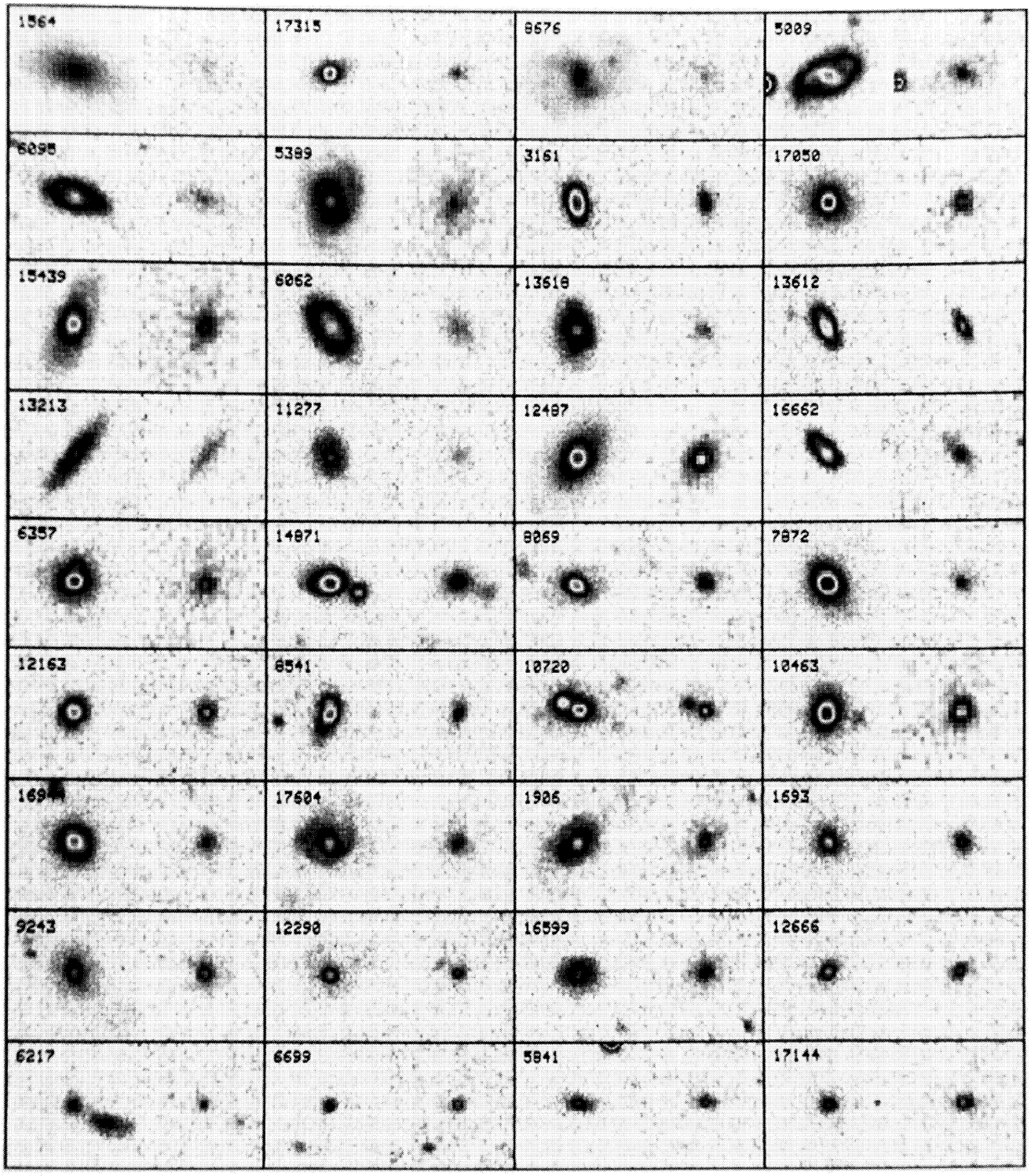

(d)

FIG. 16. (d) fm spectral-type galaxies.

Bershady *et al.* (see page 892)

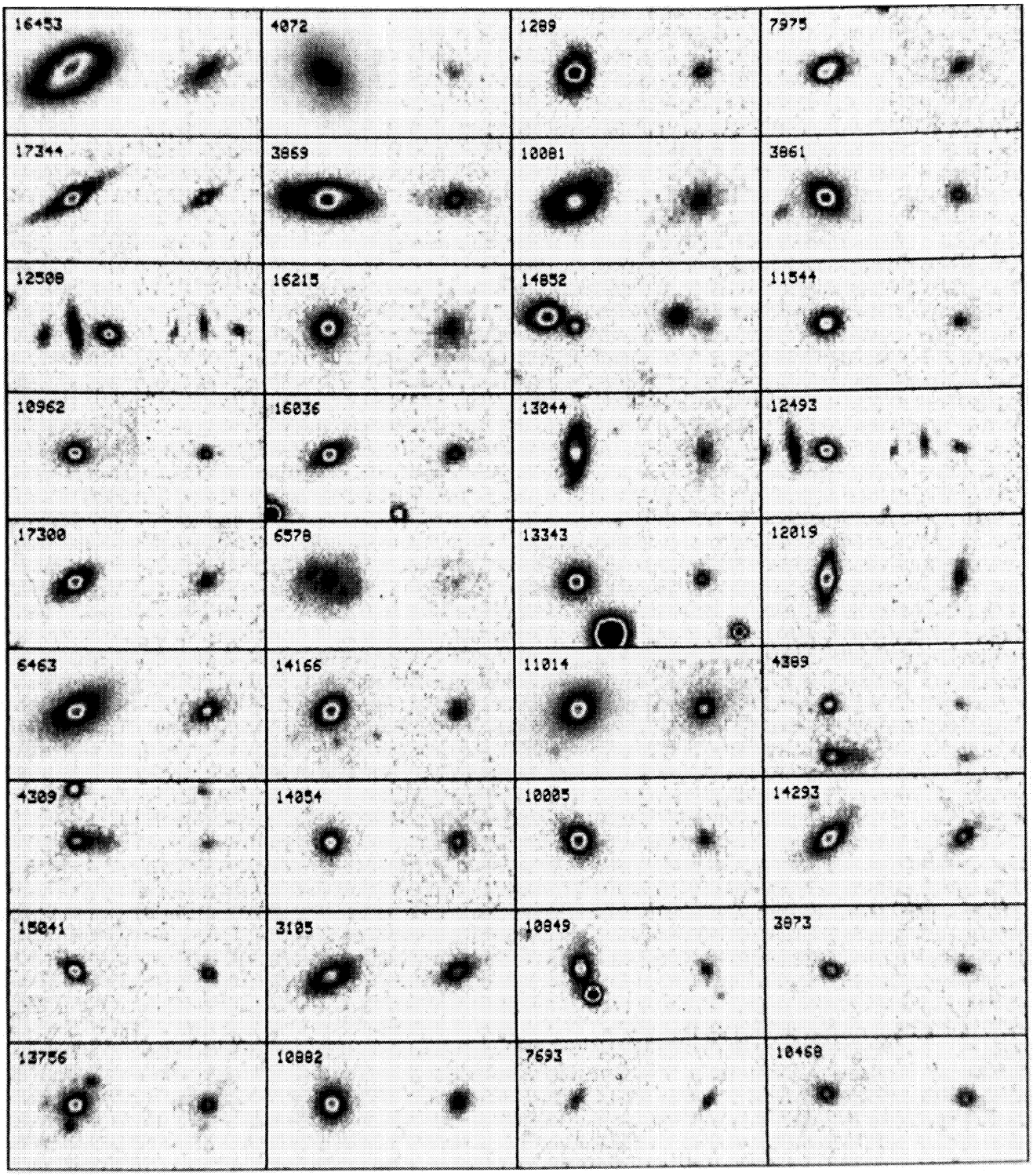

(e)

FIG. 16. (e) gm spectral-type galaxies ($z<0.229$).

Bershady *et al.* (see page 892)

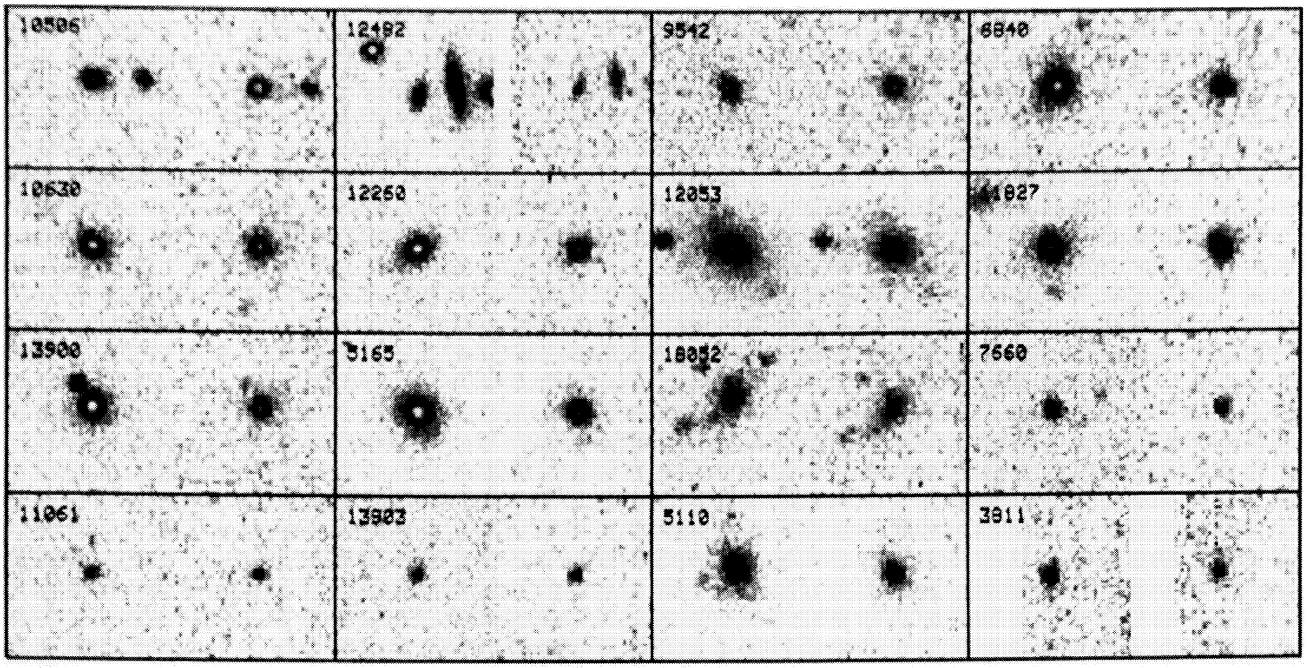

(f)

FIG. 16. (f) gm spectral-type galaxies ($z \geqslant 0.229$).

Bershady *et al.* (see page 892)